Hayabusa analogue sample analysis using synchrotron imaging.

Akira Tsuchiyama[1)], Kentaro Uesugi[2)] and Tsukasa Nakano[3)]

1) Department of Earth and Space Science, Graduate School of Science, Osaka University, Toyonaka, 560-0043, Japan

2) SPring-8/Japan Synchrotron Radiation Research Institute, Mikazuki, Hyogo Prefecture, 679-5198 Japan

3) Geological Survey of Japan/National Institute of Advanced Industrial Science and Technology, Tsukuba, 305-8567 Japan

Abstruct

Densities of Hayabusa analog samples were measured without contamination using synchrotron X-ray microtomography at BL20XU of SPring-8 and an ultra-microbalance. The density of sample II-1A is 6.37±0.02 g/cm^3. The density of sample II-1B were scattered (5.05-7.18 g/cm^3). This may caused by volume estimation problem in the microtomography due to the presence of a large amount of highly absorbed materials (probably Fe-Ni metal) and less absorbed materials (probably silicates). Increment of the number of projection in the tomographic imaging will solve the problem. Three-dimensional grain size distribution of sample II-1A was obtained by identification of individual grains in the 3-D CT images. This will give the basic physical poperties of regolith, which may be present on Itokawa's surface. Several phases were recognized in the 3-D CT images using CT value histograms of the images, and their 3-D distribution maps were obtained with the spatial resolution of down to about 0.5 μm. This will helpful for planning later destructive analyses. The density, phase estimation (probably plagioclase, Fe-Mg silicates, troilte, kamacite and taenite in sample II-1A and Fe-Mg silicates, kamacite and taenite in sample II-1B if meteorites are assumed) and their modes and textures suggest possibility of an ordinary chondrite (LL is favarable) with high petrologic type for sample II-1A and a stony iron for sample II-1B although the conclusion cannot be made definitely from the CT images alone. Subtraction microradiography was also applied to sample II-1A to search Zr-bearing minerals effectively for the Pb-Pb dating. Any Zr-bearing minerals were not observed within the spatial resolution of about a few μm, but zircon grains added in sample II-1A were easily recognized by this method.

1. Introduction

X-ray computed tomography (CT) is a non-destructive method that provides cross-sectional images (CT images) of objects using X-ray attenuation. Three-dimensional (3-D) internal structures can be obtained by stacking successive CT images. A synchrotron radiation (SR) source provides tunable, monochromatized, and naturally collimated (parallel) X-ray beams that have many advantages for CT (Flannery et al. 1987; Bonse and Busch 1996). Monochromatized beams eliminate beam hardening, which causes CT image artifacts, and thus permit CT values, which correspond to the X-ray linear attenuation

coefficient (LAC) of a material obtained by tomographic reconstruction, to relate quantitatively to LACs (Tsuchiyama et al. 2005). Furthermore, collimated beams readily yield 3-D images with high spatial resolution. Uesugi et al. (1999, 2001) have developed a projection X-ray microtomographic system, named SP-μCT, using SR at SPring-8, a third generation SR facility at Nishi-harima, Hyogo Prefecture, Japan. SP-μCT has been applied to earth and planetary materials (e.g., Tsuchiyama et al. 2001, 2003ab; Nakashima et al. 2005). 3-D element images were also obtained by imaging objects just above and below the X-ray absorption edge energy of an element (the so-called "subtraction" method: e.g., Thompson et al. 1984) for Fe in a micrometeorite (Tsuchiyama et al. 2001) and Cs in a Cs-doped partially molten granite (Ikeda et al. 2004). In addition to the micotomography, we can also apply microradiography technique using SP-μCT to larger samples than those for the microtomography.

In this report, we applied the microtopmography and micoradiography at SPring-8 to Hayabusa analogue samples (HASPET samples), which were prepared by ISAS/JAXA for the second HASPET selection. 3-D structures of the samples are obtained non-destructively by the microtomography. The main purpose is to obtain the bulk densities of the samples non-destructively without contamination. In this menasurement, the densities are obtained from the volumes based on the 3-D structures and the masses, which are measured by an ultra-microbalance (>0.1 μg). This will be compared with the average density of Itokawa, which will be measured during ran-de-vous of the spacecraft with Itokawa, to estimate the internal structure of the asteroid in connection with the rubble pile model (Britt et al. 2003). It should be noted that we cannot use the Archimedian method, a conventional method for measuring the densities of meteorites (Britt and Consolmagno 2003), because Archimedian fluids, such as water and helium, act as contaminants for the precious Hayabusa sample. Thre is also a possibility that the sample amount will be so small that the accuracy for the Archimedian method will be insufficient. The second purpose of the microtomographic analysis is to discriminate individual sample grains and obtain the size distribution and other statistical 3-D shape features, such as aspect ratios, of the grains. This will give basic physical properties of regolith, which may be present on the Itakawa's surface. The third purpose is to describe the 3-D structures of some individual grains for planning later destructive analysis by sectioning the samples, such as SEM and TEM observations and many chemical analyses. As a CT image is expressed as a spatial distribution of CT values and the constituent minerals can be estimated based on the CT values, we can roughly estimate 3-D distributions of minerals.

Specific phases, where some important elements are concentrated, can be searched by the subtraction method. Although subtraction microtomography will give 3-D distribution of the specific minerals (Tsuchiyama et al., in preparation), the sample volume is restricted if high spatial resolution is required. In contrast, larger amounts of samples can be used with high resolution by microradiography. Another purpose of this study is to search Zr-bearing minerals, such as zircon and badeleite, effectively for age determination using the Pb-Pb mehod and some highly-refractory minerals with platinum element group, Mo, W etc. In the present study, only Zr-bearing minerals were searched due to the limited beam time at SPring-8.

2. Experiments

Imaging experiments using SP-μCT are available at three different beamlines, BL20B2, BL20XU and BL47XU, mainly depending on the sample size. The effective spatial resolutions are about 13 μm at BL20B2 for samples smaller than 5 mm in diameter (Uesugi et al. 1999) and about 1 μm at BL20XU and BL47XU for samples smaller than 0.45 mm in diameter (Uesugi et al. 2001). The present HASPET samples were imaged at BL20XU and BL20B2. However, as the sample sizes are so small that the samples were not suitable for imaging at BL20B2, only the results at BL20XU are reported here.

Two kinds of samples were sent from ISAS/JAXA: II-1A is a fine powder sample (<~100 μm in size) in gray color (Figure 1) and II-1B is composed of rounded dark gray grains (a few tens to a few hundreds μm in size) (Figure 38). Single or multiple grains attached on glass fibers or powders in Al capsules were imaged. Glycole phthalate was used as a glue to stick sample grains on the top of a glass fiber of 5 or 200 μm in diameter. Glycole phthalate can be easily removed by acetone without any serious contamination even for noble gas measurements (Tomoki Nakamura, a personal communication). A list of samples and their imaging conditions are summarized in Table 1. Some of the sample mass were measured by an ultra-microbalance (Sartorius SC-2: >0.1 μg). Each mass was measured six times and the average and standard deviation were calculated. The ample preparation and the mass measurement was carried out in a clean room at Osaka University.

2-1. Micotomography

SP-μCT is composed of an X-ray source, a sample stage, and an X-ray beam monitor (Fig. A1). Details of the system is essentially the same as that described in Tsuchiyama et al. (2005). Images of transmitted X-ray intensities through a sample were taken at X-ray energies of 10 to 30 keV depending on the size of the samples. The samples were rotated by 180 degrees with a rotational step angle of 0.12 degrees (1500 projections). Images of direct X-ray beams with no sample (I_0 images) and dark current of the detector system were measured by thirty times respectively, before and after the CT measurement for correction of the images. All images were obtained by an X-ray detector, where the X-ray was transformed into visible light by a fluorescent screen, expanded by a relay lens and subsequently detected by a cooled CCD camera (2000 × 1312 format with a full well of 13000 electrons). The sample and fluorescent screen were positioned as close together as possible (~1 mm) to avoid X-rays refracted by the sample. Imaging required 1 to 5 hrd depending on the X-ray energy and sample size. After the standard pre-processing of raw X-ray intensities and their logarithm conversions, CT images (2000 × 2000 pixels in full images) were reconstructed by a convolution back-projection algorithm (Nakano et al. 1997, 2000) with a Chesler's type convolution filter. 3-D structures were reconstructed by stacking 200-1312 slice images. Two long samples were imaged three times after moving the samples vertically in each time (041009d, e and f for II-1A-P1 and 041009g, h and I for II-1A-P2). The size of each cubic voxel (pixel in 3-D) in the 3-D images was 0.195, 0.47 or 0.948 μm, and the effective spatial resolution was about 0.5 to a few μm depending on the pixel size.

Sample portions in 3-D images were extracted by using threshold of CT values. The threshold values

were determined from CT value histograms (frequency diagram of CT values) of the 3-D images. The threshold values were adopted as mean values of the representative CT values for phases, which are determined by peaks or bumps of the histograms (e.g., see Figure 4). Validity of taking the mean value as the threshold was checked by some materials with known densities (mineral grains and powder of glass beads). The densities were well reproduced by this threshold within the errors of about 3% (Hurukawa, 2005). The volumes of the solid samples, each phase and internal voids were calculated from the numbers of voxels those belong to the phases or voids and the voxel size (0.195^3, 0.470^3 or 0.948^3 μm: Table 1). The modes of the phases were estimated from the volumes. Image analysis was carried out using 3-D image analysis tool, SLICE (Tsuchiyama et al., 2005). We can also estimate phases from the CT values because LAC is a physical property as a function of the bulk density and the chemical composition of a material and X-ray energy. If the monochromatic beam is used CT values should be ideally equal to LACs. However, they are not identical due to non-linearity of the system (Tsuchiyama et al., 2005). Qualitative CT value - LAC relation was determined at BL20B2 by imaging standard materials (Tsuchiyama et al., 2005). Prior to the HASPET sample imaging, CT value - LAC relation was determined at BL20XU to estimate real LAC values from CT values. The results are shown in Appendix (LAC = 0.8850(0.0110) × CT value: Fig. A2). Phases in the HASPET samples were estimated from the CT values (and thus LAC values) with the relation. The compositions of solid solutions (e.g., Fo content of oliviene) were also roughly estimated from the CT values.

2-2. Microradiography

Powder samples (II-1A) were sandwiched between Al foils of about 1 x 1 cm for searching Zr-bearing minerals by subtraction microradiography (Fig. 50). Projection images were measured at X-ray energies just above and below the Zr K-edge (18.04 and 17.98 keV). Each image has 2000 × 800 format with the pixel size of 0.948 μm (about 1.9 × 0.76 mm^2). Mosaic images of the samples were formed by tiling multiple projection images (55 and 60 images). X-ray transmittance ($q = (I-I_d)/(I_0-I_d)$, where I, I_0, and I_d are the X-ray intensities of transmitted, inciodent and dark beams, respectively). Images expressed by q were obtained for the two set of images, and subtraction images from the q images were obtained. The subtraction of the transmittance, Δq, is expressed as $\exp(-\mu_1 S)-\exp(-\mu_2 S)$, where μ_1 and μ_2 are LACs at below and above the edge energy and S is the sample thickness. $\mu = \rho \sum_i w_i \tau_i(E)$, where w_i is the weight fraction of element-i and τ_i is the mass attenuation coefficient (MAC) as a function of X-ray energy, E. If the X-ray energy interval at above and below the Zr K-edge is small, only τ_{Zr}'s are different, and thus, Zr-bearing materials should have $\Delta q>0$ and other materials have $\Delta q=0$.

If a mineral grain is at a Bragg angle, the contrast of this grain is affected by the Bragg reflection. In order to check this possibility, another set of projection images were measured by rotating the samples by 1 degree. Stereographs were also made from the two sets of images with different angles.

3. Results and Discussion

The results are briefly summarized in Table 2.

3-1. Tomographic study of sample II-1A

(a) Sample II-1A-009ag-B10

Sample II-1A-009ag-B10 is an aggregate of grains attached on a glass fiber (Fig. 2). A browse image, where CT images at some slices are shown, is given in Figure 3. The left bar in the browse image shows the size scale in cm, and the right bar shows the gray scale of CT value in cm^{-1}. Brighter objects have larger CT values or larger X-ray absorption and *vise versa*. A glass fiber of about 200 μm in diameter is also seen in the slices 0462, 0617, 0722 and 0927. Absorption by glycole phthalate (glue) is so small that it is expressed as very dark object although the surface can be recognized as a slightly bright curve as refraction contrast (e.g., slice 0927 in Figure 3). Four phases were recognized form the CT images and its CT value histogram (Figure 4: in this histogram pixel value, PV, of 16 bit CT images is used in stead of CT values for convenience for image analysis because the image analysis was made using the 16 bit CT images). Clear peaks were recognized at 6.10 and 107.6 cm^{-1}, which are attributed to phases-A and C, respectively. Two bumps were also recognized at about 32.95 and 115.3 cm^{-1}, which are attributed to phases-B and D, respectively. If representative minerals in meteorites are assumed, the phases-A, B, C and D should be Fe-Mg silicates (olivine and/or orthopyroxene), troilite, kamacite and taenite (Table 3). The Fo and En contents of olivine and orthopyroxene , respectively, and Fe/(Fe+Ni) ratios of kamacite-taenite were roughly estimated in Table 3 too. It should be noted that the errors of the compositions are large (Fo91 probably means Fo80-100 or relatively Mg-rich olivine), and the accurate compositions should be determined by EPMA. It is also noted that we cannot discriminate olivine and orthopyroxene (and clinopyroxene also) in CT images due to overlapping of their LACs.

3-D distribution of the phases (Figure 5) was obtained from CT value threshold, which is taken as the mean value of the two peaks (Figure 4). The mode of each phase was estimated from this 3-D distribution (Table 4). If phases-A and B are in contact, thin regions with the intermediate CT values, which are recognized wrongly as phase-C, appear artificially between them in CT images (e.g., see concentric distribution of phases-A, B and C in Figure 5b). Therefore, the mode of phase-C might be overestimated. However, the roughly estimated modes can be used as tentative values. 3-D information about the rough distribution will contribute to later destructive analysis by sectioning the samples. The accuracy of the mode will be increased by increasing the number of projection in the tomographic imaging. The volume of the bulk solid should not have such large error. However, the density was not obtained for this sample because the mass was not measured. If the density obtained for other powders of the same sample (3.67 g/cm^3) is adopted, the mass should be 0.075 mg.

Each grain was also identified in this sample by image analysis procedure. The results are shown in Fig.5c, where the glass fiber was removed from the CT images manually. In this image, grains with different color sjow different grains. However, only seven colors are used to recognize individual grains, different grains may have the same color. In fact, three red and three yellow grains in Figure 5c are different grains. Bird's eye view of the sample is shown in Figure 6. A plaster model, enlarged accurately

from the 3-D CT images, can be made using rapid prototyping method (Tsuchiyama et al., 2003b). Statistics of the grain size and shape was obtained from the information about the individual grains. Grain size was calculated as the diameter of a sphere with the same volume of a grain. The size distribution is shown as a histogram of the grain size (in ϕ scale) in Figure 7 and a cumulative frequency diagram in Figure 8. The distribution shows that similar to log-normal distribution although the size range and number of grains are small. Some parameters for the size distribution were also calculated (Table 5). If a grain is approximated as a three-axis ellipsoid, the major, intermediate and minor axis length (A>B>C) can be calculated. Figure 9 shows the plot of the axial ratios, C/B vs. B/A for different sizes. The grains are equally distributed in the prolate (C/B>B/A) and oblate regions (C/B<B/A), and the aspect ratio (C/A) ranges from about 0.4 to 0.9.

(b) Sample II-1A-P1 and P2

These samples are filled in Al capsules (Fig. 10). Browse images are shown in Figures 11 and 17. Combined successive CT images were made from the CT images by three imaging experiments. Bird's eye views and vertical sliced CT images are shown in Figures 14 and 15 for II-1A-P1 and Figures 19 and 20 for II-1A-P2, respectively. In the bird's eye views, the Al capsules were removed manually. However, the inner surface portions were slightly remains as thin films (Figure 14 and 19). CT value histogram for the sample regions (Figure 12) shows that the phases and their modes are consistent with those estimated from the sample II-1A-009gr-B10 (Tables 6 and 7, see also Table 2). Distribution of the phases is shown in Figures 13 and 18. The densities of the samples were calculated from the masses and volumes. This density corresponds to grain density and was 3.67 (0.02) g/cm^3 (Table 7).

In this sample, a large amount of fine particles are present in the large irregular grains as seen in Figures 13b and 18b. We have tried to identify individual grains in the samples, but some grains were not separated clearly due to the fine grains and close contact of irregular grains. In contrast, we have succeeded in separating rounded particles, such as beach sands. Separation of closely packed irregular shaped grains remains as feature issue.

(c) Sample II-1A-001-A1, 002-A2, 003-A3, 004-A4, 005-A5, 006-A6 and 010-A14

A single grain was picked up and attached to a glass fiber of 5 μm in diameter (Figures 21 and 22). The masses were not measured for the small grains. From the volumes, we can estimate the masses using the average density of 3.67 g/cm^3 (Table 9). Some can be measured by the ultra-microbalance. On the other hand, we can image these small samples with the highest spatial resolution (0.195 μm voxel size: Table 1). Based on the CT images and CT value histogram (Figure 23), one additional phase, which has smaller CT values than the "Fe-Mg silicates", was recognized. The CT values can be explained by plagioclase. Plagioclase and Fe-Mg silicates were not discriminated well in the previous samples imaged with relatively lower spatial resolution. Because the LAC range of the plagioclase solid solution is narrow (77.6 and 49.9 cm^{-1} for anorthite and albite, respectively), a large error should be included in the An contents in Table 8. Browse images, phase distribution maps and bird's eye views of individual grains are shown in Figures 24-33. There are some variations of the modes of the phases, the averaged modes are consistent with the previous ones (Table 9, see also Table 2). The mode of "plagioclase" is about 10 vol.%. Some blur is present in the periphery of large metal grains (e.g., Figure 35a). This might cause overestimation of

plagioclase mode (Figure 35b). Plagioclase is present as interstitially between Fe-Mg silicate crystals (e.g., Figures 32 and 33). The size of the plagioclase grains are the order of 100 μm or smaller. Detailed 3-D structures of the grains with this high spatial resolution will help further destructive analyses.

(d) What is sample II-1A?

It is impossible to conclude definitely the material of the sample based on CT images alone. However, we can give some speculation on this sample if the sample is assumed to be a meteorite. The density, texture and estimated phase are not inconsistent with an ordinary chondrite with high petrologic type, such as 6. The measured density (3.67 g/cm^3) is mostly similar to the average density of H condrite (3.64 g/cm^3: Britt and Consolmagno, 2003), but we cannot exclude the possibility of L and LL chondrites if we consider the range of the density of individual chondrites (Table 2). If the modes of troilite and metal are taken into considered, LL chondrite is favorable. Strictly speaking, possibility of a primitive achondrite, such as winonaites, can not be excluded.

3-2. Tomographic study of sample II-1B

All the samples imaged are a single grain attached on 200 μm glass fibers (Figures 39 and 40). Sample II-1B-002-A8, 004-A10 and 008-A15 were imaged at 30 keV and II-1B-001-A7 at 25 keV. As the samples consists of large amounts of materials with very high LACs (phases-B and C) and relatively low LACs (phase-A) (Figures 41 and 48), there are no best X-ray energies, which gives clear CT images. Especially, there are noise in phase-A and blur near the surface of pahses-B and C (Figures 43b, 46b, 47b and 49b). The images at 25 keV, where the peak of phase-A can be recognized in the CT value histogram (Figure 48), is better than those at 30 keV, where only bumps are recognized (Figure 39). At any rate, the volumes obtained from the 3-D CT images are not so accurate compared with sample II-1A. The density is about 6.9 g/cm^3 for the 30 keV samples and 5.1 g/cm^3 for the 25 keV sample (Tables 11 and 13, respectively, and see also Table 2). The modes of phase-A are different and this causes the density difference. We do not know the discrepancy is due to the energy difference or merely variation of individual grains.

The CT values suggest that phases-A, B and C should be Mg-rich silicate(s), kamacite and taenite , respectively (Tables 10 and 12). Troilite may be present as shown in Figure 49a, where materials with intermediate brightness between phases-A and B are present although there is not any peak or bump in the CT value histogram (Figure 48). The metal grains are rounded and the size is the order of 100 μm. Any Widmanstatten structures were not observed.

The above features suggest that the sample is a stony iron meteorite. The grain size of the sample is smaller than most of pallasites. The density (5.1-6.9 g/cm^3) is larger than that of pallasirte (4.76 g/cm^3: Britt and Consolmagno, 2003). An Eagle station pallasite might be possible for the grain size. Some silicate inclusions in iron meteorites might be another possibility.

3. Radiographic study of sample II-1A

Figure 51 shows mosaic images of sample II-1A-P3. We can observe many grains as well as Al foils in the projection images at above and blow the Zr K-edge energy. Any bright spots were not seen in the subtraction image, suggesting Zr-bearing phase within the spatial resolution of the image (about a few μm)

is absent in this sample. In contrast, many zircon grains are easily recognized in the subtraction image of sample II-1A-P4z, where zircon grains were added to II-1A powder. Figure 53 shows stereographs of close up of sample II-1A-P4z. The same bright spots are present in the two subtract images with different beam angles by 1 degree. This shows that all the bright spots are not due to Bragg reflection contrast but due to Zr contrast.

We have already applied this subtraction method to an eucrite (Millbillillie) for searching zircon crystals in meteorites using tomography (Tsuchiyama et al., in preparation). We observed large zircon grains of up to 60 μm. in a 3.2 mm^3 sample. Therefore, this technique will be also useful to the samples returned from Itokawa.

4. Acknowledgement

This study is possible only at SPring-8 in Japan. The authors are grateful to Dr. Yoshio Suzuki of JASRI/SPring-8. We also thank to Mrs. Kentaro Nakamura and Hirokazu Furukawa of Osaka University for their helps. Especially, Mr. Nakamura obtained the CT value – LAC relation at BL20B.

References

Bonse, U. and Busch, F. (1996) X-ray computed microtomography (μCT) using synchrotron radiation (SR). Progress in Biophysics and Molecular Biology, 65, 133-169.

Britt, D.T. and Consolmagno, G. (2003) Stony meteorite porosities and densities: a review of the data through 2001. Meteoritics and Planetary Science, 38, 1161-1180.

Britt, D.T., Yeomans, D., Housen, D., and Consolmagno, G. (2003) Asteroid density, porosity, and structure. Asteroid III, 485-500.

Flannery, B.P., Deckman, H.W., Roberge, W.G., and D'Amico, K.L. (1987) Three-dimensional X-ray microtomography. Science, 237, 1439-1444.

Hurukawa H. (2005) Density measurement and estimation of minerals in Hayabusa analog samples. Bachelor thesis at Osaka University. In Japanese.

Ikeda, S., Nakano, T., Tsuchiyama, A., Uesugi, K., Suzuki, Y., Nakamura, K., Nakashima, Y. and Yoshida, H. (2004) Nondestructive three-dimensional element-concentration mapping of a Cs-doped partially molten granite by X-ray computed tomography using synchrotron radiation. American Mineralogist, 89, 1304-1312.

Nakano, T., Nakamura, K., Someya, T. and Ohtsuka, H. (1997) Observation of 3-dimensional internal structures of rock using X-ray CT: (1) density calibration of CT value (in Japanese with English abstract). Geoinformatics, 8, 239-255.

Nakano, T., Nakashima Y., Nakamura, K. and Ikeda, S. (2000) Observation and analysis of internal structure of rock using X-ray CT (in Japanese with English abstract). Journal of Geolical Society of Japan, 106, 363-378.

Nakashima, Y., Nakano, T., Nakamura, K., Uesugi, K., Tsuchiyama, A., and Ikeda, S. (2004)

Three-dimensional diffusion of non-sorbing species in porous sandstone: computer simulation based on X-ray microtomography using synchrotron radiation. *Jour.* Contaminant Hydrology, 74, 253-264.

Thompson, A.C., Llacer, J., Campbell Finman, L., Hughes, E.B., Otis, J.N., Wilson, S. and Zeman, H.D. (1984) Computed tomography using synchrotron radiation. Nuclear Instruments and Methods in Physics Research, 222, 319-323.

Tsuchiyama, A., Uesugi, K., Noguchi, T., Yano, H., Nakano, T. and Suzuki, Y. (2001) Three-dimensional microstructures of Antarctic micrometeorites by X-ray computed tomography using synchrotron radiation at SPring-8. Meteoritics and Planetary Science, 36, Suppl. A210.

Tsuchiyama, A., Shigeyoshi, R., Kawabata, T., Nakano, T., Uesugi, K. and Shirono, S. (2003a) Three-dimensional structures of chondrules and their high-speed rotation. Lunar and Planetary Science Conference, XXXIV, Abstract #1271, Lunar and Planetary Institute, Houston (CD-ROM).

Tsuchiyama, A., Osada, Y., Nakano, T. and Uesugi, K (2003b) Experimental reproduction of classic barred olivine chondrules: open system behavior and thermal history of chondrule formation. Geochimica et Cosmochimica Acta., 68, 653-672.

Tsuchiyama, A., Uesugi, K., Nakano, T., and Ikeda, S. (2005) Quantitative evaluation of attenuation contrast of X-ray computed tomography images using monochromatized beams. American Mineralogist, 90, 132-142.

Uesugi, K., Tsuchiyama, A., Nakano, T., Suzuki, Y., Yagi, N., Umetani, K. and Kohmura, Y. (1999) Development of micro-tomography imaging system for rock and mineral samples (presented at the SPIE Conference on Developments in X-Ray Tomography II, Denver, Colorado, July, 1999). Proceedings of Society of Photo-Optical Instrumentation Engineers, 3772, 214-221.

Uesugi, K., Suzuki, Y., Yagi, N., Tsuchiyama, A. and Nakano, T. (2001) Development of high spatial resolution X-ray CT system at BL47XU in SPring-8. Nuclear Instruments and Methods in Physics Research A, 467-468, 853-856.

Table 1. A list of samples and conditions for the present imaging experiments.

beam line	imaging no.	sample	sample form and its containor	energy (keV)	exposure (sec)	number of projection	number of I_0 image	number of dark image	pixel size (μm)	remarks
BL20XU	041007e	II-1A-009ag-B10	aggregate on glass fiber	25	0.25	1500	30	30	0.47	
BL20XU	041009d	II-1A-P1-1*	powder in Al capsule(1.0/1.5ϕ)	25	0.2	1500	30	30	0.948	
BL20XU	041009e	II-1A-P1-2*	powder in Al capsule(1.0/1.5ϕ)	25	0.2	1500	30	30	0.948	upper region of 041009d by 600μm
BL20XU	041009f	II-1A-P1-3*	powder in Al capsule(1.0/1.5ϕ)	25	0.2	1500	30	30	0.948	upper region of 041009e by 600μm
BL20XU	041009g	II-1A-P2-1*	powder in Al capsule(1.0/1.5ϕ)	25	0.2	1500	30	30	0.948	
BL20XU	041009h	II-1A-P2-2*	powder in Al capsule(1.0/1.5ϕ)	25	0.2	1500	30	30	0.948	upper region of 041009g by 500μm
BL20XU	041009i	II-1A-P2-3*	powder in Al capsule(1.0/1.5ϕ)	25	0.2	1500	30	30	0.948	upper region of 041009h by 500μm
BL20XU	041008b	II-1A-005-A5	single grain on glass fiber	10	0.25	1500	30	30	0.195	
BL20XU	041008c	II-1A-004-A4	single grain on glass fiber	10	0.25	1500	30	30	0.195	
BL20XU	041008d	II-1A-003-A3	single grain on glass fiber	10	0.25	1500	30	30	0.195	
BL20XU	041008e	II-1A-002-A2	single grain on glass fiber	10	0.25	1500	30	30	0.195	
BL20XU	041008f	II-1A-001-A1	single grain on glass fiber	10	0.25	1500	30	30	0.195	
BL20XU	041008h	II-1A-006-A6	single grain on glass fiber	10	0.25	1500	30	30	0.195	
BL20XU	041008i	II-1A-010-A14	single grain on glass fiber	10	0.25	1500	30	30	0.195	
BL20XU	041007a	II-1B-004-A10*	single grain on glass fiber	30	0.25	1500	30	30	0.47	
BL20XU	041007b	II-1B-008-A15*	single grain on glass fiber	30	0.25	1500	30	30	0.47	
BL20XU	041007c	II-1B-002-A8*	single grain on glass fiber	30	0.25	1500	30	30	0.47	
BL20XU	041008a	II-1B-001-A7*	single grain on glass fiber	25	0.25	1500	30	30	0.47	
BL20XU	041010a	II-1A-P3, II-1A-P4z	powder wrapped in Al foil	18.04, 17.98	0.2	55-60	30	30	0.948	radiography for seraching Zr-bearing minerals using subtraction method
		* mass measured								

Table 2. Brief summary of the present report.

sample No.	**009ag-B10**	**P1, P2**	**001-006,010**			
imaging No.	**041007e**	**041009def, ghi**	**041009b,c,d,e,f,h,i**			
sample	**grain aggregate**	**powder**	**grain**			
grain density (g/cm^3)	**n.d.**	**3.67(0.02)**	**n.d.**	**3.64(0.12)**	**3.51(0.11)**	**3.48(0.08)**
bulk density (g/cm^3)				**3.40(0.18)**	**3.35(0.16)**	**3.21(0.22)**
mode (%)						
plagioclase			**12.0(5.2)**			
Mg-Fe silicates	**91.2**	**95.5(0.1)**	**85.5(7.7)**			
troilite	**4.9**	**3.2(0.2)**	**1.5(3.0)**			
Fe-Ni metal	**3.8**	**1.3(0.3)**	**0.4(1.3)**			
kamacite	**3.7**	**1.1(0.2)**	**0.4(1.3)**			
taenite	**0.1**	**0.2(0.0)**				
void	**n.d.**	**n.d.**	**0.6(0.4)**	**6.0(4.5)**	**5.8(4.7)**	**9.3(8.5)**
composition						
plagioclase (An)			**63-100**			
olivine (Fo)	**91**	**87**	**84-93**			
orhtopyroxenen (En)	**88**	**82**	**77-90**			
kamacite (Fe/Fe+Ni)	**69**	**86**				
taenite (Fe/Fe+Ni)	**50**	**57, 36?**				
HASPET sample	**II-1B**	**II-1B**		**pallasites***	**mesosiderites***	
sample No.	**002,004,008**	**001**				
imaging No.	**041007a,b,c**	**041008a**				
sample	**grain**	**grain**				
grain density (g/cm^3)	**6.89(0.29)**	**5.05(0.32)**		**4.76(0.10)**	**4.40(0.36)**	
bulk density (g/cm^3)				**4.49(0.53)**	**4.25(0.02)**	
mode (%)						
plagioclase						
Mg-Fe silicates	**37.7(2.7)**	**67.3**				
troilite		**32.7**				
Fe-Ni metal	**62.3(2.7)**					
kamacite	**61.4(3.1)**					
taenite	**0.9(0.7)**					
void	**n.d.**	**n.d.**		**0.0(0.52)**	**3.0(8.1)**	
composition						
plagioclase (An)						
olivine (Fo)	**83**	**89**				
orhtopyroxenen (En)	**76**	**85**				
kamacite (Fe/Fe+Ni)	**88**	**97**				
taenite (Fe/Fe+Ni)	**43**					
				*** Britt and Consolmagno (2003)**		

HASPET sample II-1A: OM images

(a)

II-1A_x40.JPG

(b)

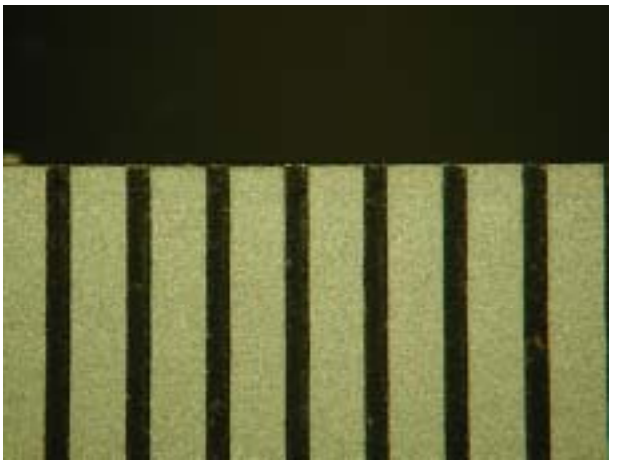

scale_x40.JPG (0.5 mm)

(c)

II-1A_x90.JPG

(d)

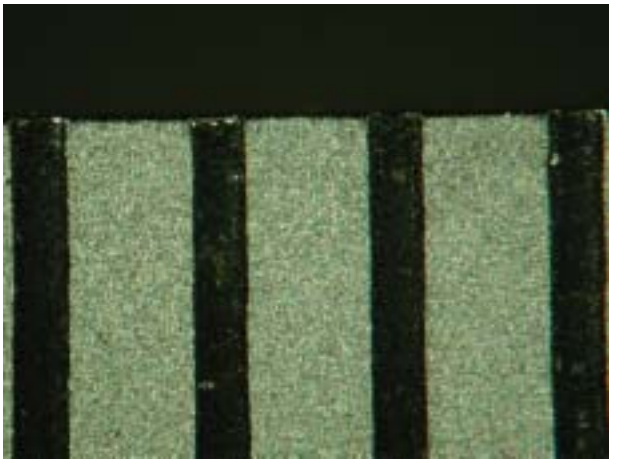

scale_x90.JPG (0.5 mm)

Figure 1. Photomicrographs of HASPET sample II-1A. (a) Low magnification. (b) A scale for (a). The separation between each scale bar is 0.5 mm. (c) High magnification. (d) A scale for (c). The separation between each scale bar is 0.5 mm.

II-1A-009ag-B10 (041007e): OM image and browse image

(a)

II-1A-009ag_B10_x40.JPG

(b)

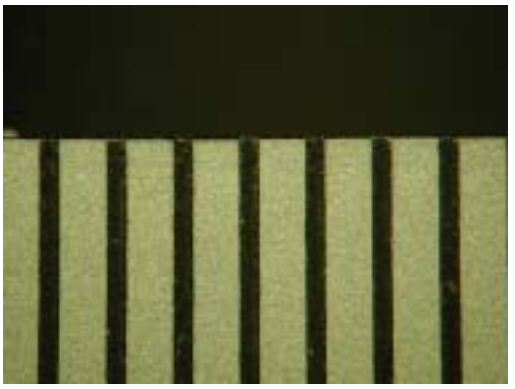

scale_x40.JPG (0.5 mm)

Figure 2. A photomicrograph of HASPET sample II-1A-009ag-B10 (041007e). (a) A powder sample is attached on a glass fiber with glycole phthalate. (b) A scale for (a). The separation between each scale bar is 0.5 mm.

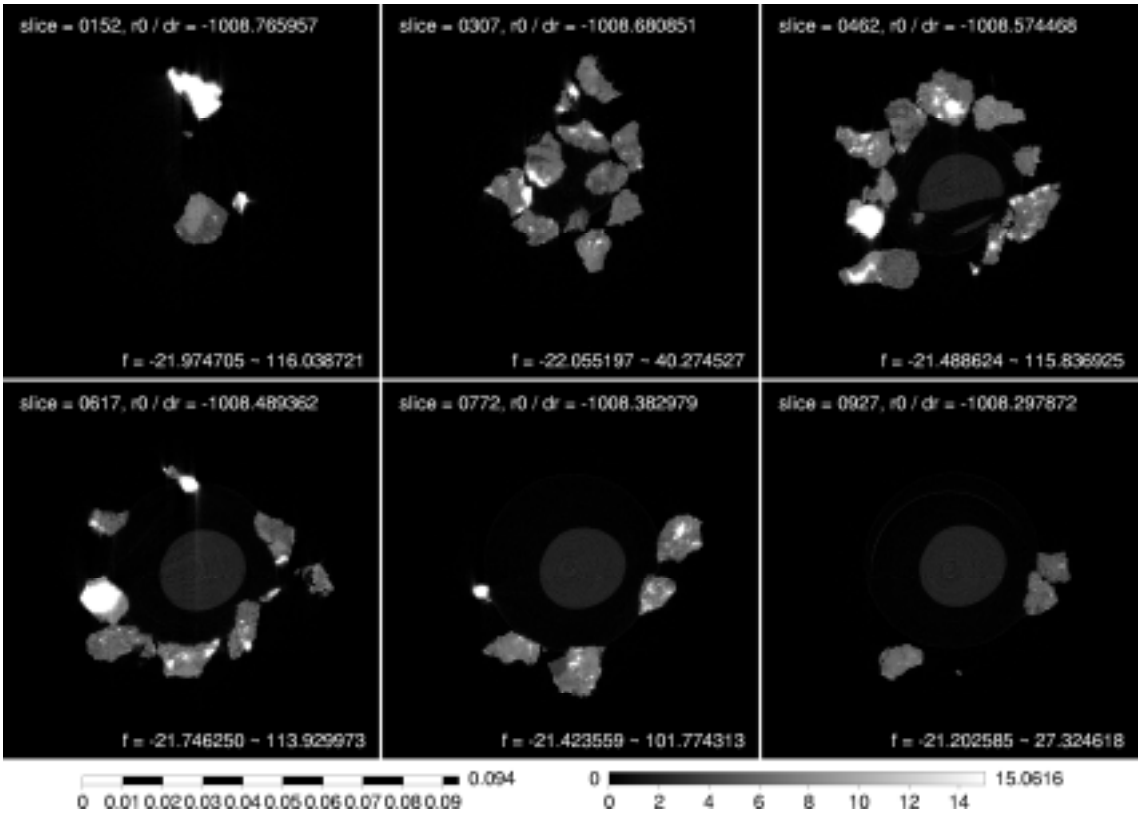

Figure 3. A browse image of CT slices of HASPET sample II-1A_009ag-B10. The left and right bars are a scale bar in cm and a gray scale bar for CT values in cm^{-1}, respectively.

Figure 4. A CT value histogram of HASPET sample II-1A-009ag-B10. The CT values, *f*, are replaced by the pixel values, PV, in 16 bit images (f = 0.019733 cm^{-1} x PV). Peak PVs and CT values for phases-A, B, C and D, and threshold PVs between the phases are shown.

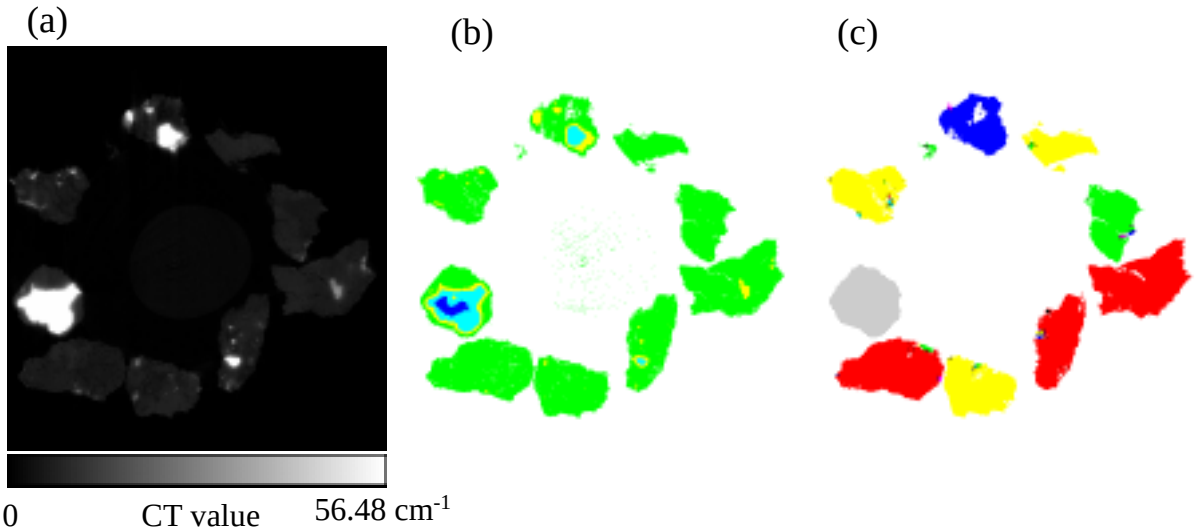

Figure 5. A typical CT slice of HASPET sample II-1A-009ag-B10. (a) A CT image (56.48 cm^{-1} corresponds to PV=2862 in Figure 4. The width of the image is 663.64 μm. (b) An image showing phases. Green: phase-A (probably Mg-Fe silicates), yellow: phase-B (probably troilite), cyan: phase-C (probably kamacite, and blue: phase-D (probably taenite). (c) An image showing individual grains. A glass fiber, which holds sample grains, was removed manually.

II-1A-009ag-B10 (041007e): bird's eye view

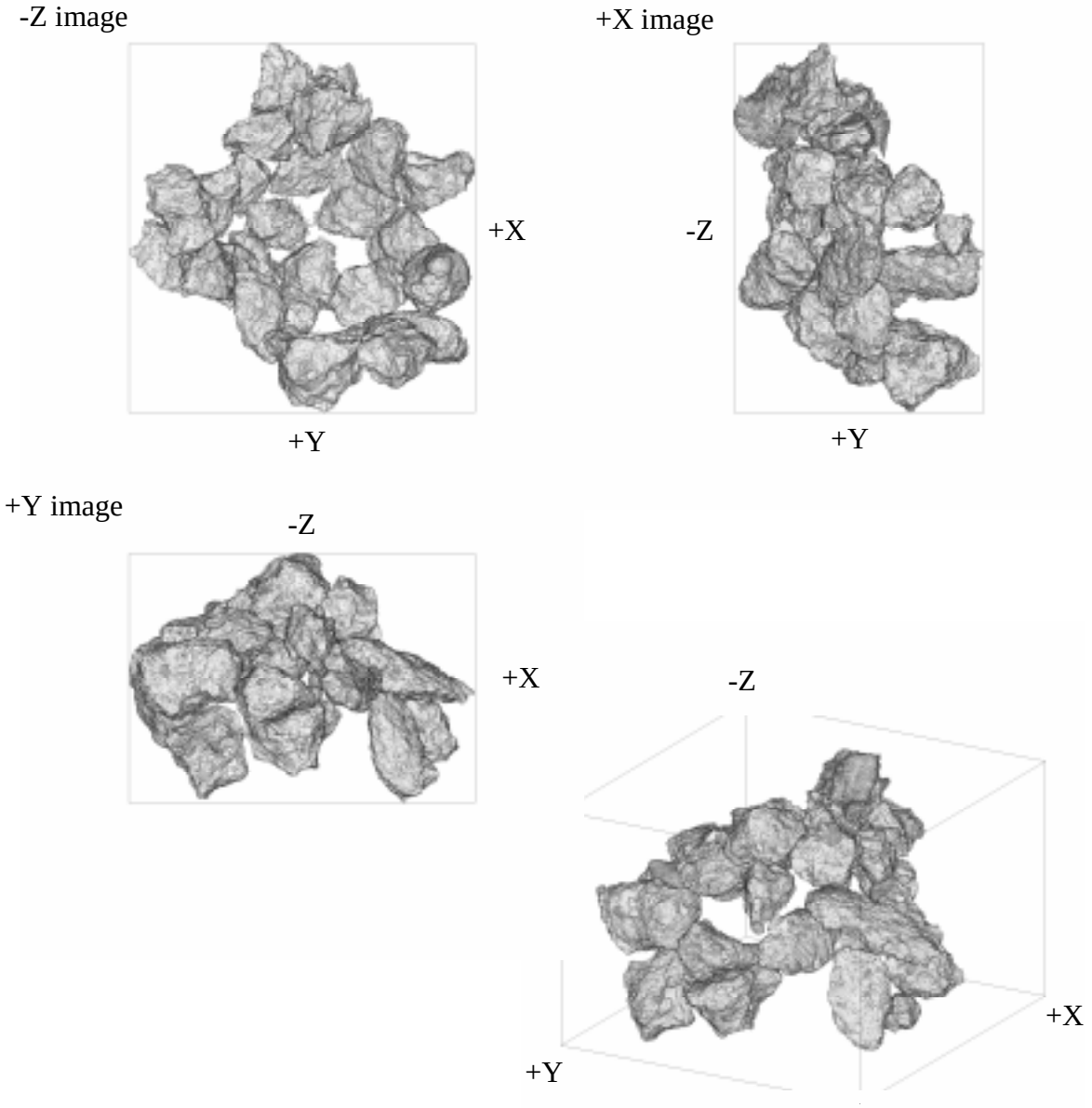

Figure 6. Bird's eye view of HASPET sample II-1A-009ag-B10. The sample size of the sample is about 660x700x470 μm. A glass fiber, which holds sample grains, was removed manually.

II-1A-009ag-B10 (041007e): grain statistics

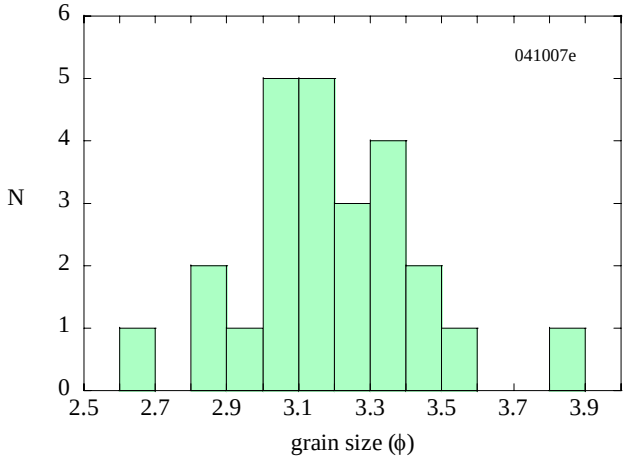

Figure 7. A histogram of grain size (in ϕ scale) of HASPET sample II-1A-009ag-B10.

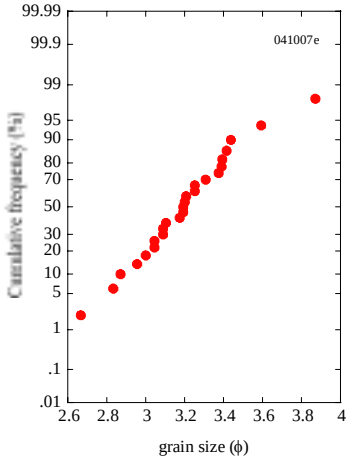

Figure 8. A cumulative frequency of grain size (in ϕ scale) of HASPET sample II-1A-009ag-B10.

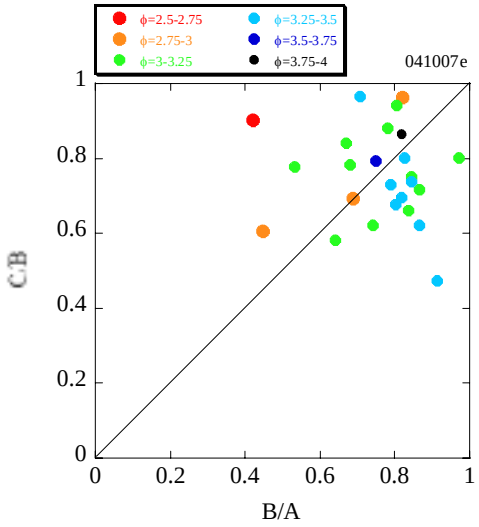

Figure 9. Grain shape distribution of HASPET sample II-1A-009ag-B10. Grains are regarded as three-axial ellipsoids (A>B>C) and the axial ratios, C/B and B/A are plotted.

II-1A-009ag-B10 (041007e): summary

Table 3. The LACs of phases-A, B, C and D in HASPET sample II-1A-009ag-B10, calculated form their CT values and estimation of their mineral candidates and compositions.

	CT value (cm^{-1})	LAC (cm^{-1})	candidates		LAC (cm^{-1})		LAC (cm^{-1})
phase-A	6.10	6.89	silicate	Fo91	6.89	En88	6.89
phase-B	32.95	37.24	trolite	troilite	48.25		
phase-C	107.64	121.63	kamacite	Fe69	121.61		
phase-D	115.34	130.33	taenite	Fe50	130.32		

Table 4. The volume of HASPET sample II-1A-009ag-B10 and the modes of the phases.

	041007e	
sample(mg)	n.d.	
stdev	n.d.	
volume (voxel)	24737545	
volume (cm^3)	2.055E-05	
density (g/cm^3)	n.d.	
stdev	n.d.	
mode (%)		candidates
phase-A	91.2	silicates
phase-B	4.9	troilite
phases-C and D	3.8	Fe-Ni metal
phase-C	3.7	kamacite
phase-D	0.1	taenite

Table 5. Statistics of grain size distribution in HASPET sample II-1A-009ag-B10.

number of grains	25	
median diameter	54.70	μm
arithmatic mean	55.27	μm
geometric mean	54.48	μm
maximum grain size	78.74	μm
minimum grain size	34.18	μm
skewness	0.407	
kurtosis	1.206	

II-1A-P1 (041009d,e and f): OM image and browse image

(a) (b)

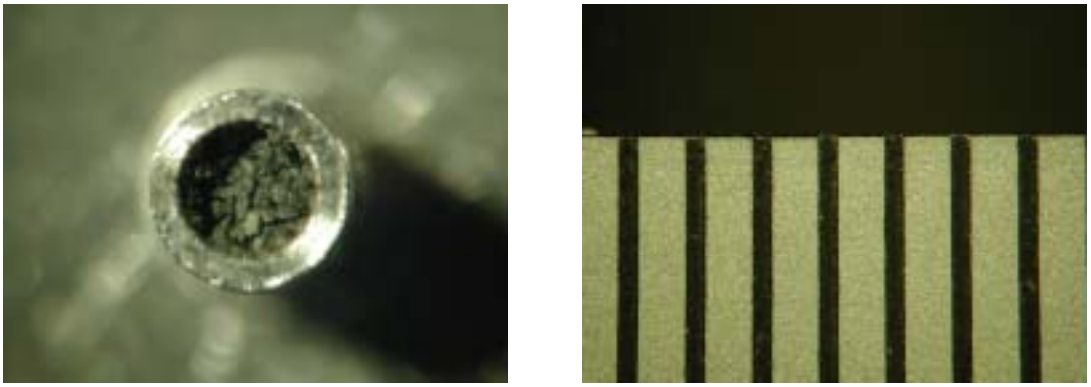

II-1A-P1_x40.JPG scale_x40.JPG (0.05 mm)

Figure 10. Photomicrograph of HASPET sample II-1A-P1 (041009d, e and f). (a) A powder sample is put into an Al capsule of 1.0 and 1.5 mm in inner and outer diameters, respectively and about 1.7 mm in depth. (b) A scale for (a). The separation between each scale bar is 0.5 mm.

(a) (b)

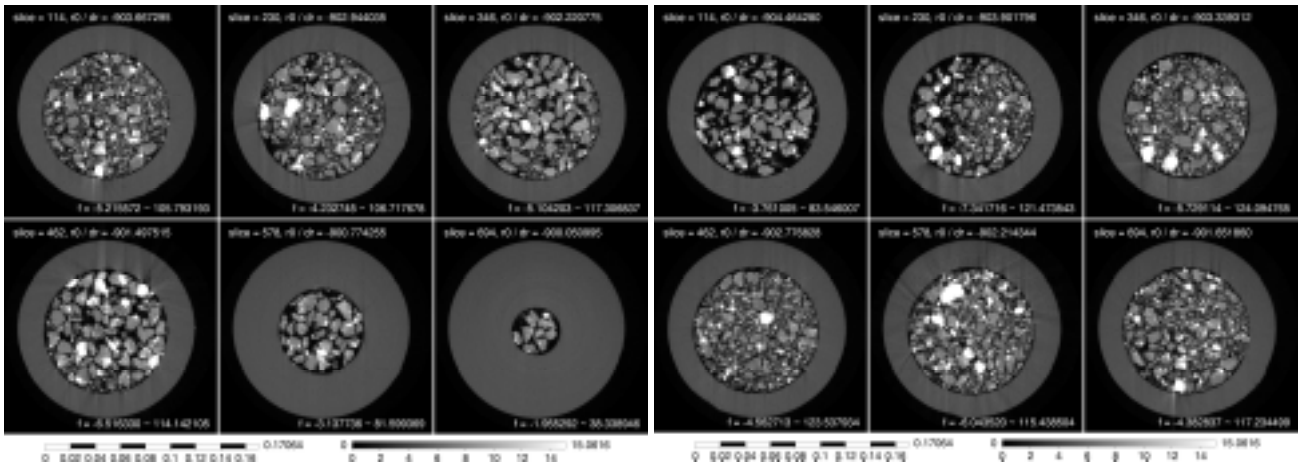

(c)

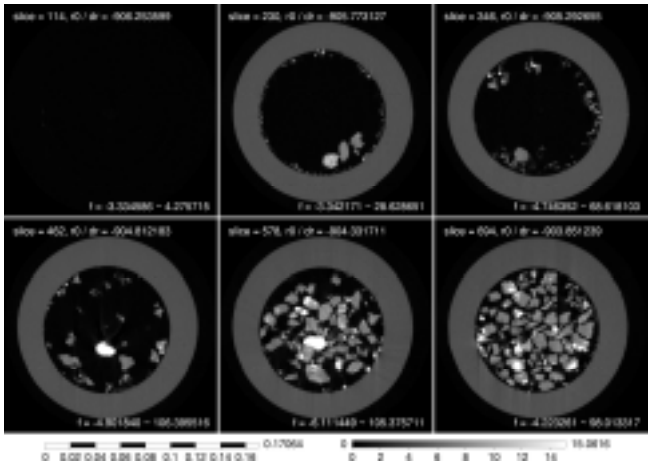

Figure 11. A browse image of CT slices of HASPET sample II-1A-P1. The left and right bars are a scale bar in cm and a gray scale bar for CT values in cm^{-1}, respectively. (a) 041009d. The bottom portion of the capsule. (b) 041009e. The middle portion of the capsule. (c) 041009f. The top portion of the capsule.

II-1A-P1 (041009d,e and f): histogram and slice images

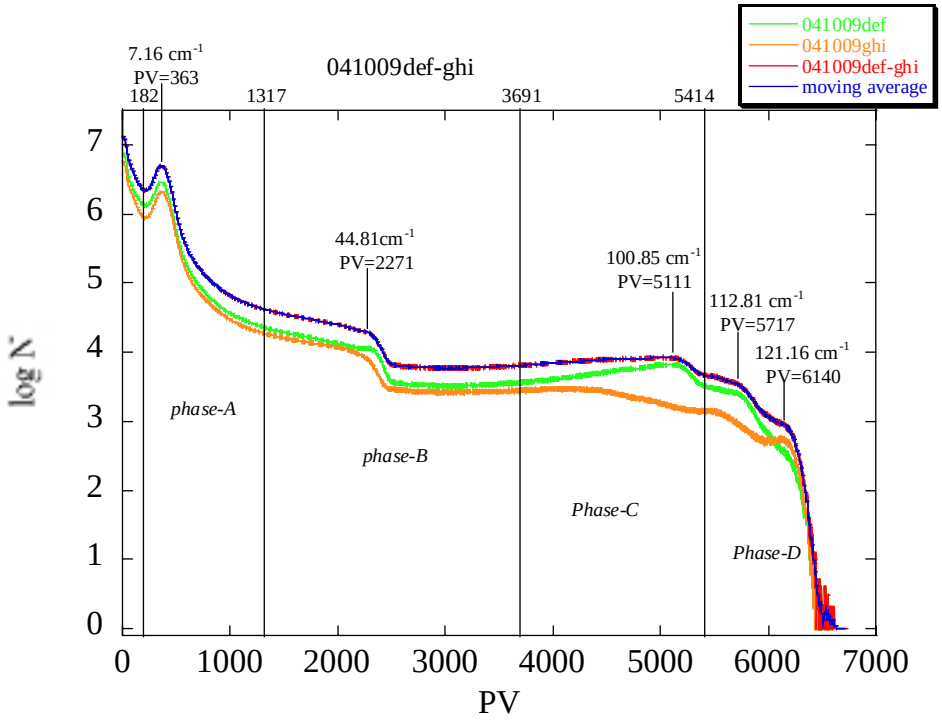

Figure 12. A CT value histogram of HASPET samples II-1A-P1 and II-1A-P2. Al capsules were removed manually. The CT values, *f*, are replaced by the pixel values, PV, in 16 bit images (*f* = 0.019733 cm^{-1} x PV). Peak PVs and CT values for phases-A, B, C and D, and threshold PVs between the phases are shown.

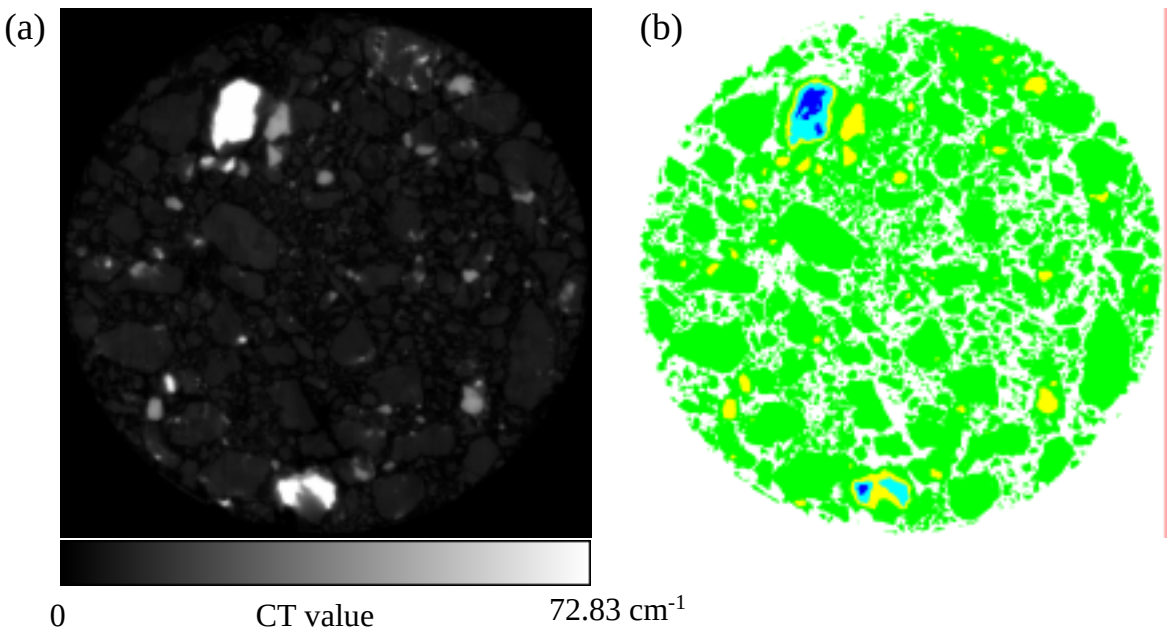

Figure 13. A typical CT slice of HASPET sample II-1A-P1. (a) A CT image (72.83 cm^{-1} corresponds to PV=3691 in Figure 12. The width of the image is 1019.5 μm. (b) An image showing phases. Green: phase-A (probably Mg-Fe silicates), yellow: phase-B (probably troilite), cyan: phase-C (probably kamacite, and blue: phase-D (probably taenite). An Al capsule was removed manually in this image.

II-1A-P1 (041007e): bird's eye view

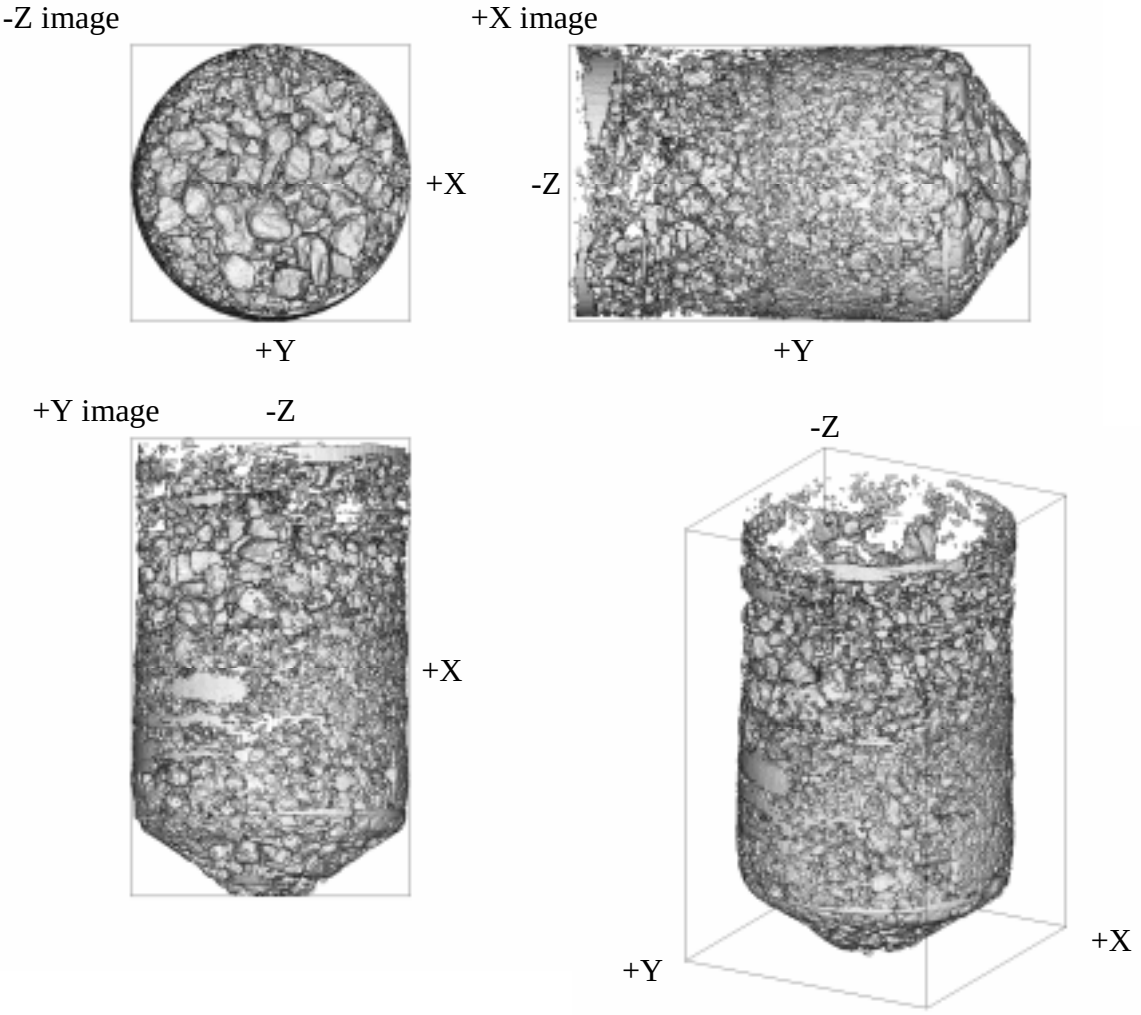

Figure 14. Bird's eye view of HASPET sample II-1A-P1. The sample size of the sample is about 1000x1000x1700 μm. An Al capsule was removed manually.

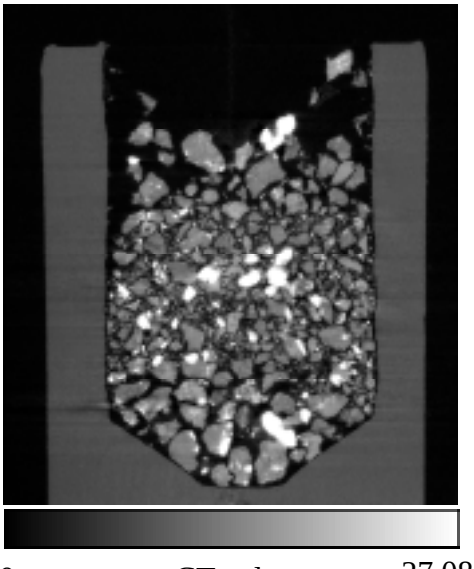

Figure 15. A CT image along a Y-Z slice of HASPET sample II-1A-P1. The image width is 1703 μm.

II-1A-P2 (041009g, h and i): OM image and browse image

(a) (b)

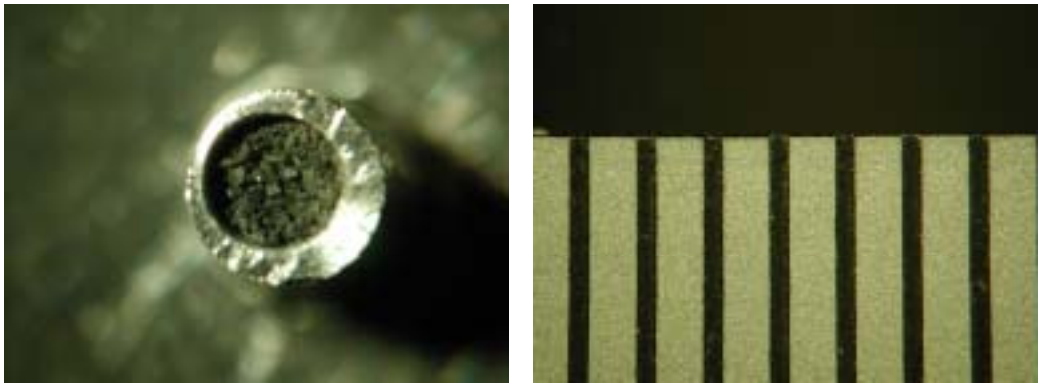

II-1A-P2_x40.JPG scale_x40.JPG (0.05 mm)

Figure 16. Photomicrograph of HASPET sample II-1A-P2 (041009g, h and i). (a) A powder sample is put into an Al capsule of 1.0 and 1.5 mm in inner and outer diameters, respectively and about 1.4 mm in depth. (b) A scale for (a). The separation between each scale bar is 0.5 mm.

(a) (b)

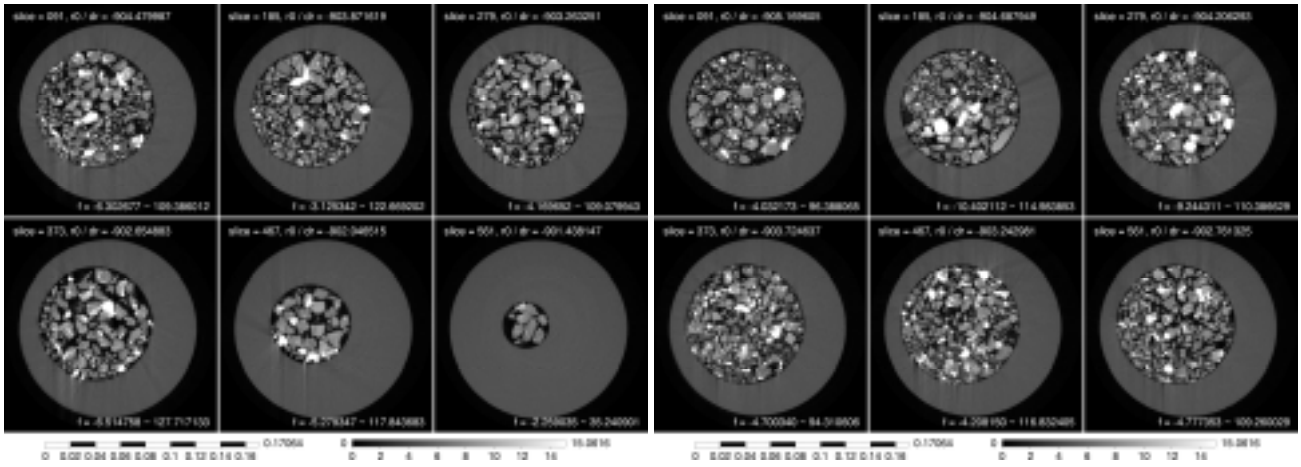

(c)

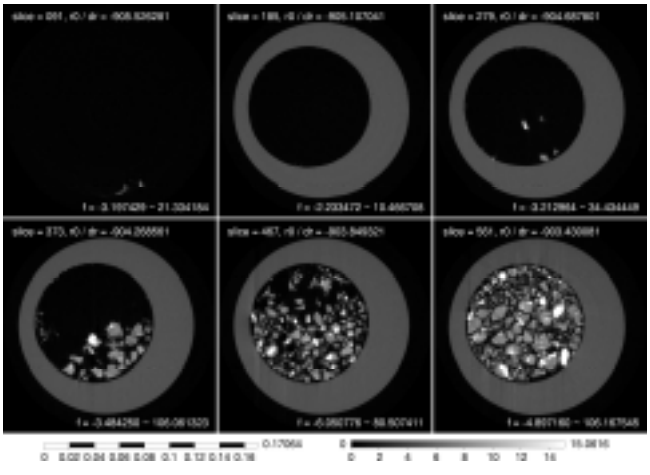

Figure 17. A browse image of CT slices of HASPET sample II-1A-P2. The left and right bars are a scale bar in cm and a gray scale bar for CT values in cm^{-1}, respectively. (a) 041009g. The bottom portion of the capsule. (b) 041009h. The middle portion of the capsule. (c) 041009i. The top portion of the capsule.

II-1A-P2 (041009g, h and i): histogram and slice images

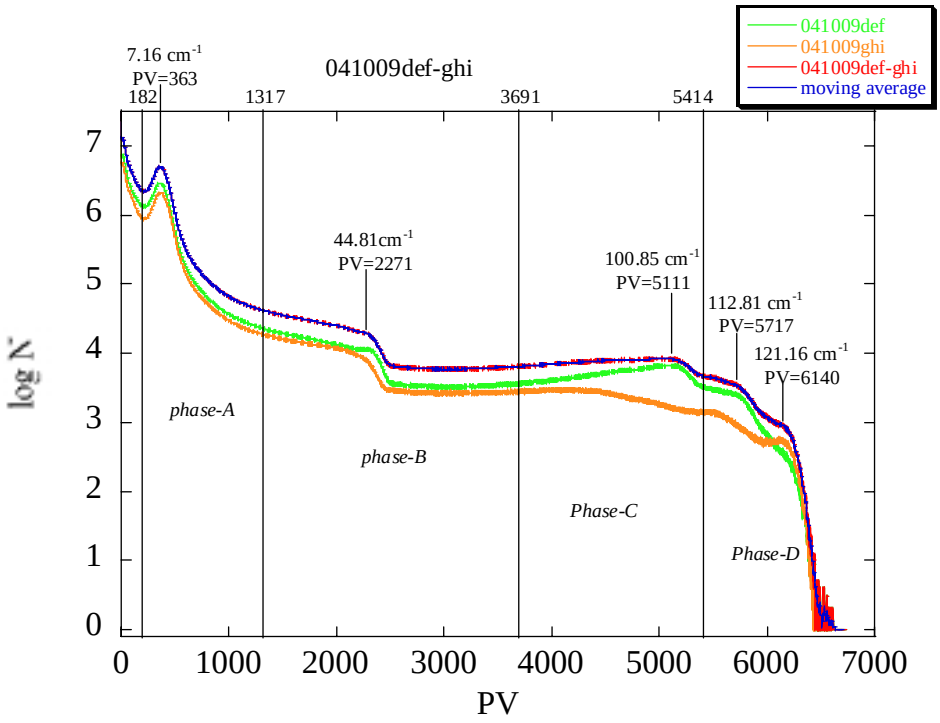

Figure 12. A CT value histogram of HASPET samples II-1A-P1 and II-1A-P2. Al capsules were removed manually. The CT values, *f*, are replaced by the pixel values, PV, in 16 bit images (f = 0.019733 cm^{-1} x PV). Peak PVs and CT values for phases-A, B, C and D, and threshold PVs between the phases are shown.

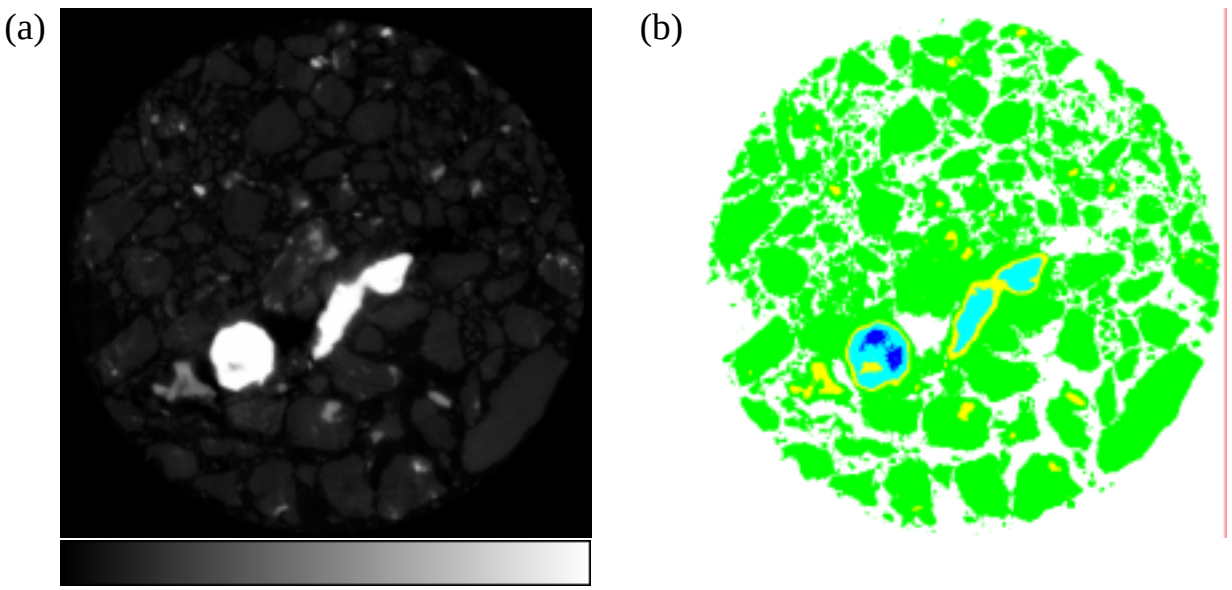

Figure 18. A typical CT slice of HASPET sample II-1A-P2. (a) A CT image (72.83 cm^{-1} corresponds to PV=3691 in Figure 12. The width of the image is 972.6 μm. (b) An image showing phases. Green: phase-A (probably Mg-Fe silicates), yellow: phase-B (probably troilite), cyan: phase-C (probably kamacite, and blue: phase-D (probably taenite). An Al capsule was removed manually in this image.

II-1A-P2 (041009g, h and i): bird's eye view

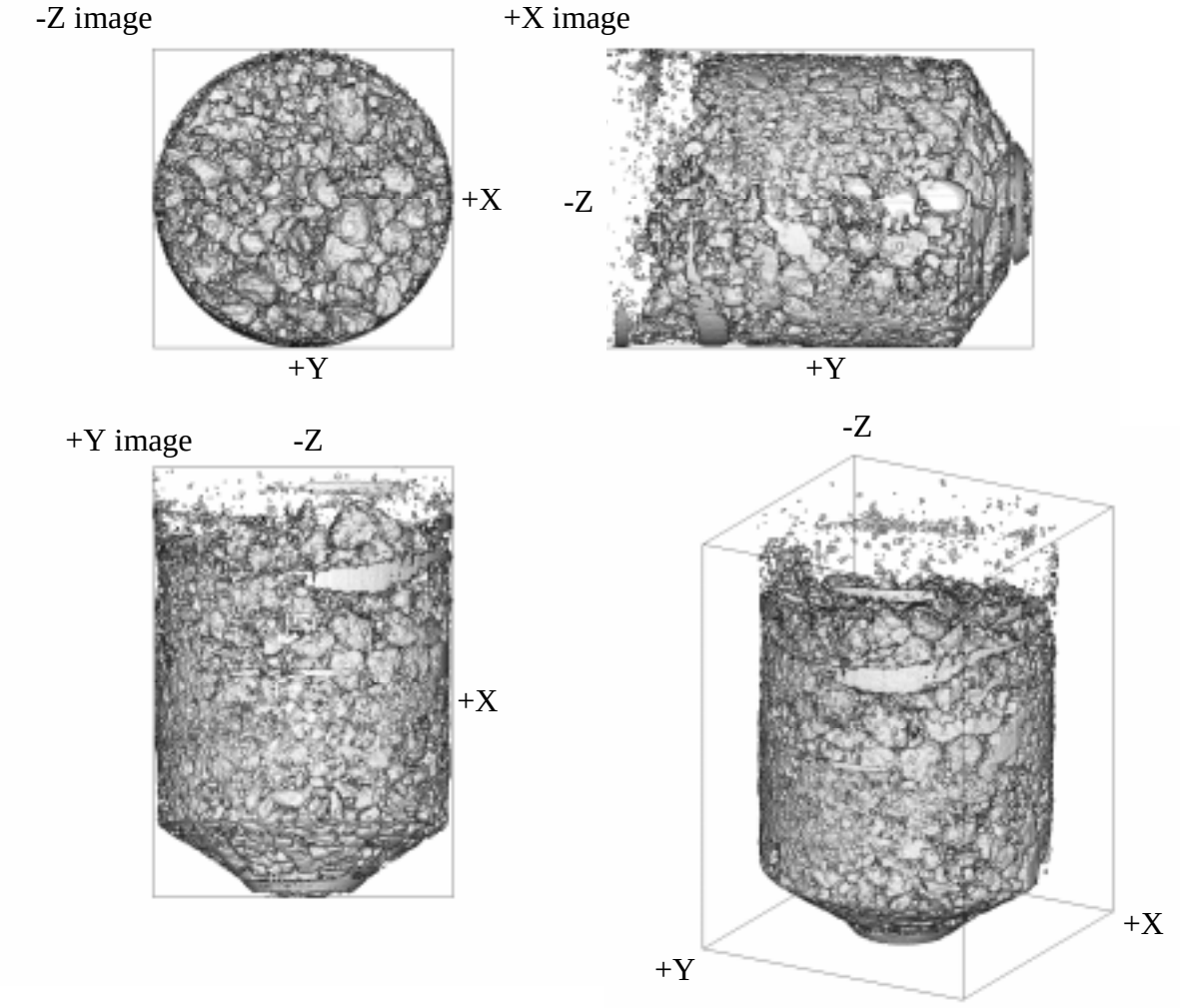

Figure 19. Bird's eye view of HASPET sample II-1A-P2. The sample size of the sample is about 1000x1000x1350 μm. An Al capsule was removed manually.

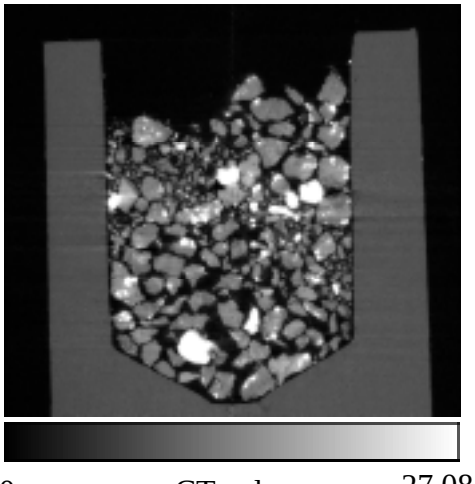

Figure 20. A CT image along a Y-Z slice of HASPET sample II-1A-P2. The image width is 1706 μm.

II-1A-P1 (041009d, e and f) and -P2 (041009g, h and i): summary

Table 6. The LACs of phases-A, B, C and D in HASPET samples II-1A-P1 and –P2, calculated form their CT values and estimation of their mineral candidates and compositions.

	CT value (cm^{-1})	LAC (cm^{-1})	candidate		LAC (cm^{-1})		LAC (cm^{-1})
phase-A	7.16	8.09	silicate	Fo87	8.09	En82	8.09
phase-B	44.81	50.64	troilite	troilite	48.25		
phase-C	100.85	113.95	kamacite	Fe86	113.96		
phase-D	112.81	127.47	taenite	Fe57	127.46		
phase-D?	121.16	136.90	taenite?	Fe36	136.89		

Table 7. The volume of HASPET samples II-1A-P1 and –P2 and the modes of the phases.

	041009def	041009ghi	wt.mean	stdev	
sample(mg)	2.1181	1.5585			
stdev	0.0003	0.0003			
volume (voxel)	680716896	497204960			
volume (cm^3)	5.800E-04	4.236E-04			
density (g/cm^3)	3.65	3.68	3.67	0.02	
stdev	0.00	0.00			
mode (%)					candidates
phase-A	95.4	95.6	95.5	0.1	silicates
phase-B	3.1	3.4	3.2	0.2	troilite
phases-C and D	1.5	1.0	1.3	0.3	metal
phase-C	1.3	0.8	1.1	0.2	kamacite
phase-D	0.2	0.1	0.2	0.0	taenite

II-1A-001 to 006, 010 (041008b, c, d, e, f, h and i). OM images

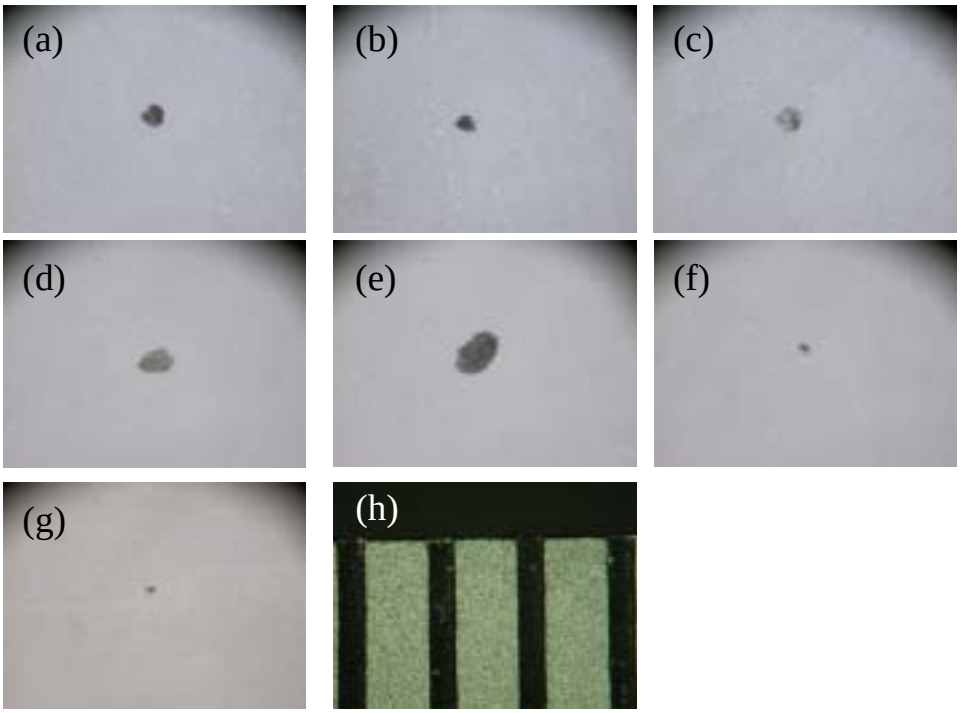

Figure 21. Photomicrograph of single grains (HASPET sample II-1A) . (a) 001-A1 (041008f). (b) 002-A2 (041008e). (c) 003-A3 (041008d). (d) 004-A4 (041008c). (e) 005-A5 (04108b). (f) 006-A6 (041008h). (g) 010-A14 (041008i). (h) A scale. The separation between each scale bar is 0.5 mm.

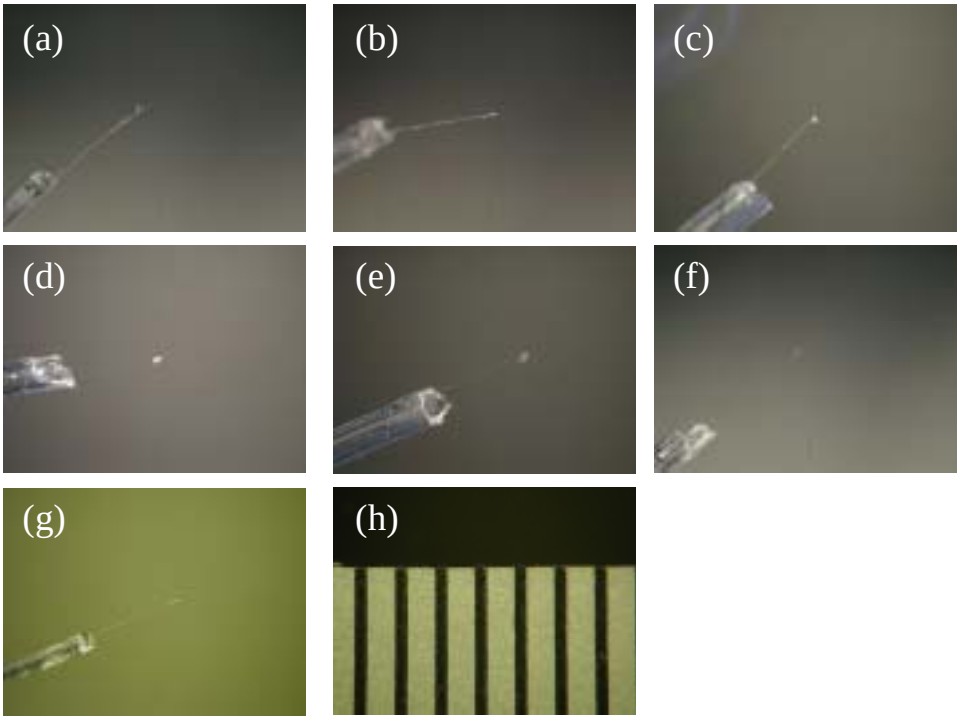

Figure 22. Photomicrograph of single grains (HASPET sample II-1A) on a glass fiber. (a) 001-A1 (041008f). (b) 002-A2 (041008e). (c) 003-A3 (041008d). (d) 004-A4 (041008c). (e) 005-A5 (04108b). (f) 006-A6 (041008h). (g) 010-A14 (041008i). (h) A scale. The separation between

II-1A-001 to 006, 010 (041008b, c, d, e, f, h and i): histogram

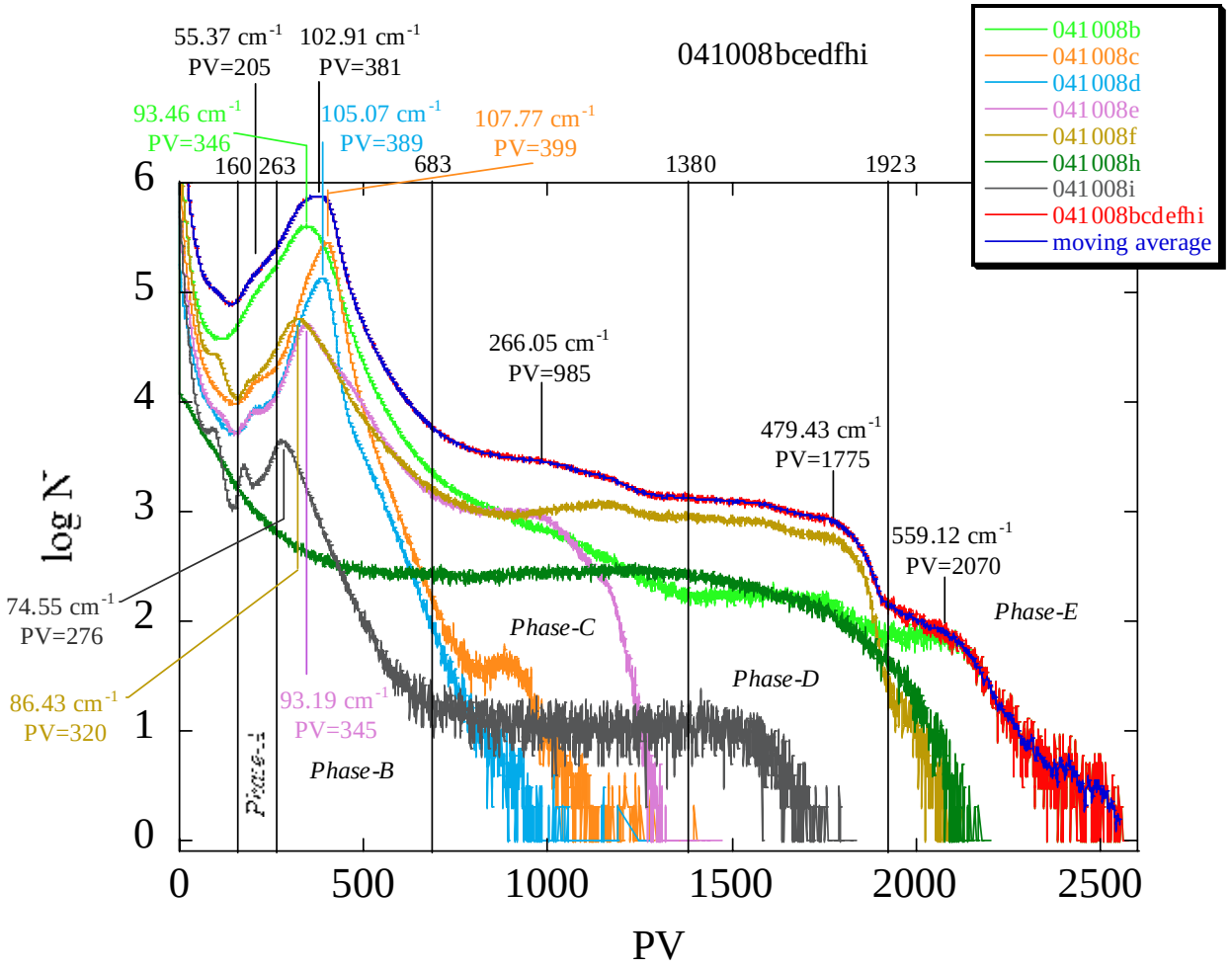

Figure 23. A CT value histogram of HASPET samples II-1A-001-A1(041008f), 002-A2 (041008e), 003-AA3 (041008d), 004-A4 (041008c), 005-A5 (041008b), 006-A6 (041008h) and 010-A14 (041008i). The CT values, *f*, are replaced by the pixel values, PV, in 16 bit images (f = 0.27010 cm^{-1} x PV). Peak PVs and CT values for phases-A, B, C, D and E, and threshold PVs between the pahses are shown.

II-1A-001-A1 (041008f): browse image, slice images, bird's eye view

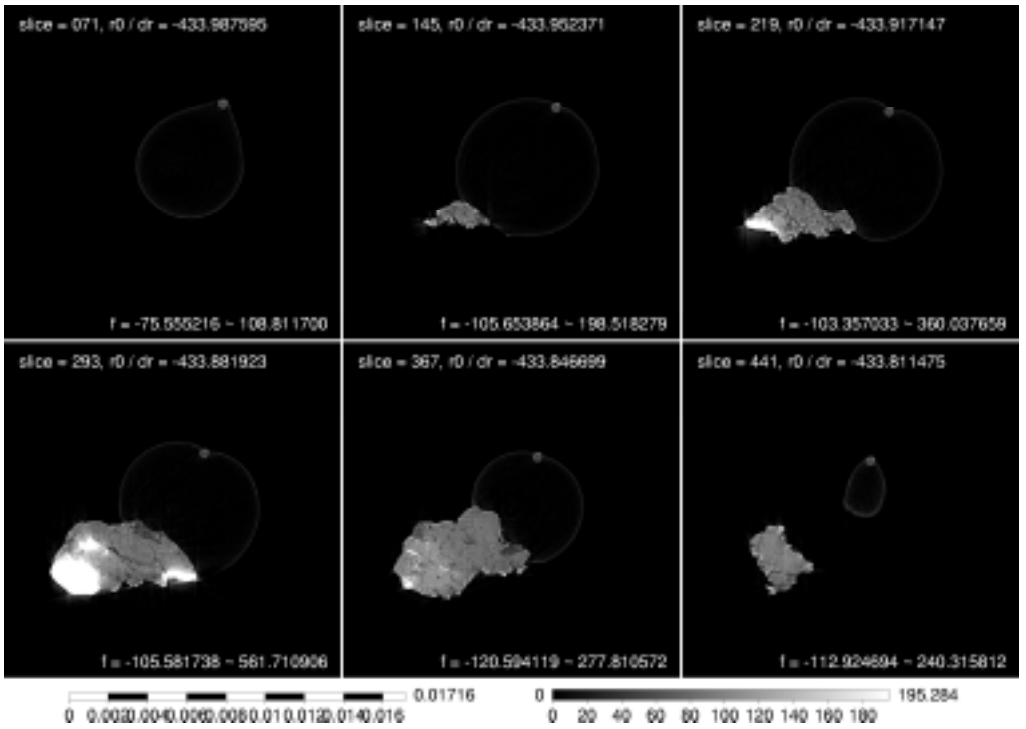

Figure 24. A browse image of CT slices of HASPET sample II-1A-001-A1 (041008f). The left and right bars are a scale bar in cm and a gray scale bar for CT values in cm^{-1}, respectively.

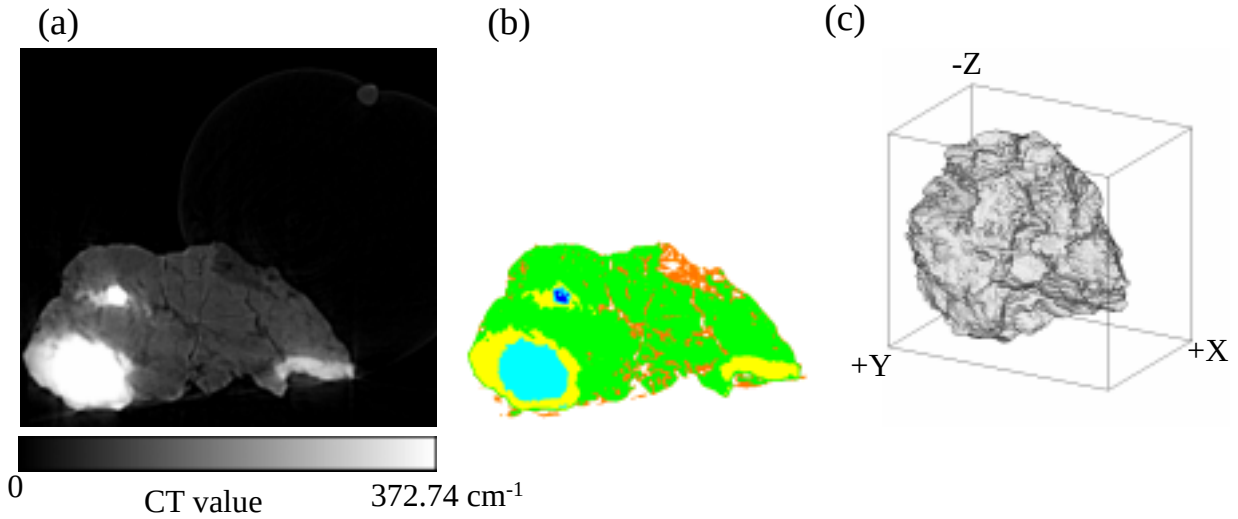

Figure 25. A typical CT slice and a bird's eye view of HASPET sample II-1A-001-A1 (041008f). (a) A CT image (372.74 cm^{-1} corresponds to PV=1380 in Figure 23. The width of the image is 95.16 μm. (b) An image showing phases. Orange: phase-A (probably plagioclase), Green: phase-B (probably Mg-Fe silicates), yellow: phase-C (probably troilite), cyan: phase-D (probably kamacite, and blue: phase-E (probably taenite). (c) A bird's eye view image (sample size: 80 x 53 x 72 μm).

II-1A-002-A2 (041008e): browse image, slice images, bird's eye view

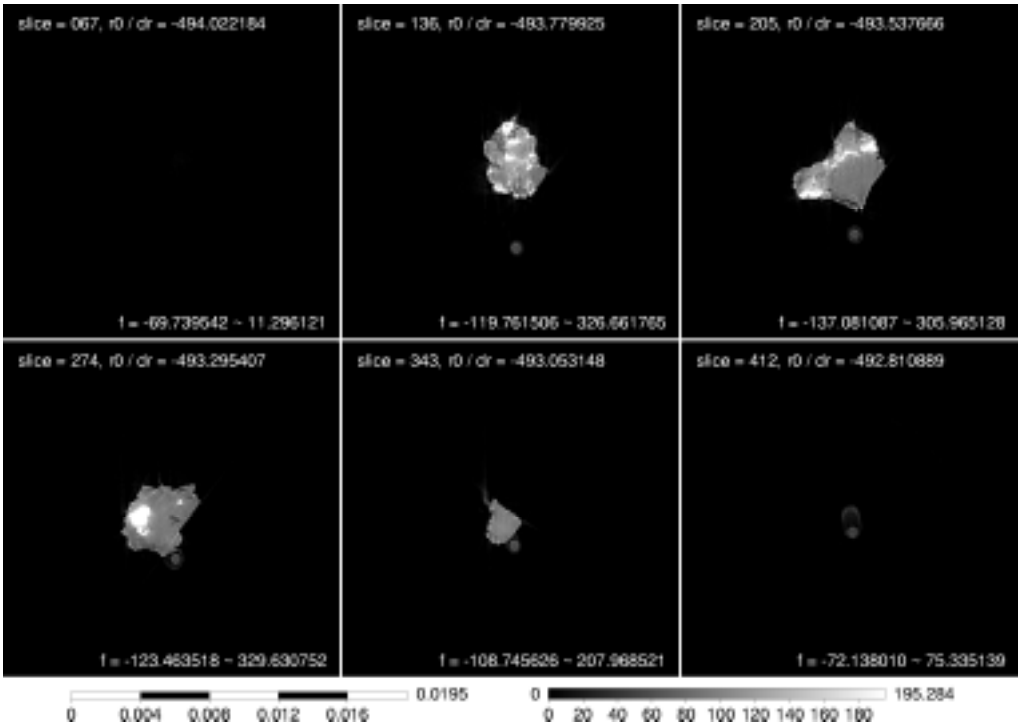

Figure 26. A browse image of CT slices of HASPET sample II-1A-002-A2 (041008e). The left and right bars are a scale bar in cm and a gray scale bar for CT values in cm^{-1}, respectively.

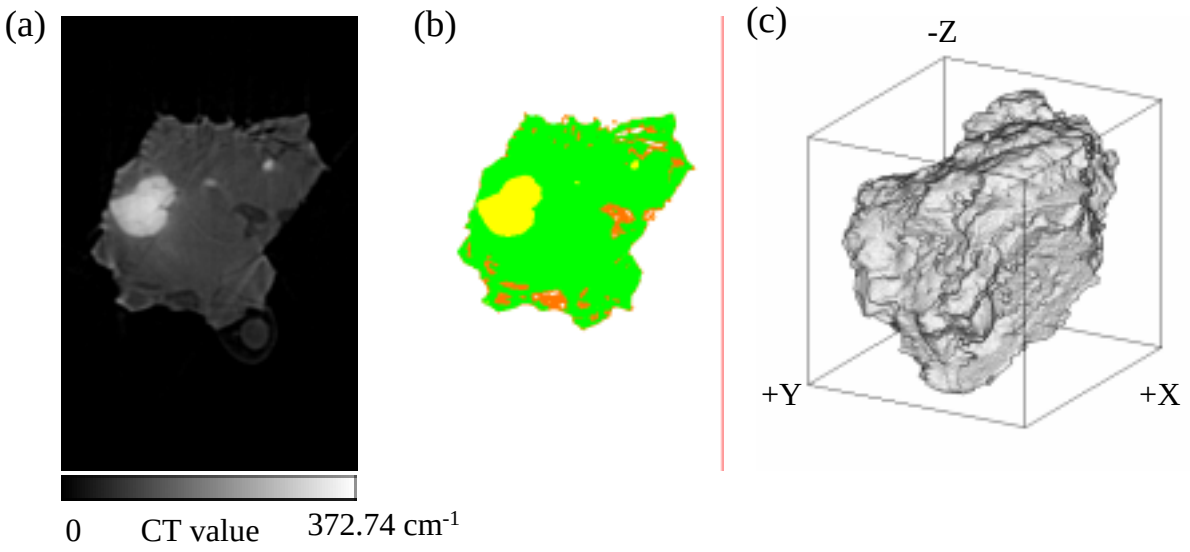

Figure 27. A typical CT slice and a bird's eye view of HASPET sample II-1A-002-A2 (041008e). (a) A CT image (372.74 cm^{-1} corresponds to PV=1380 in Figure 23. The width of the image is 56.745 μm. (b) An image showing phases. Orange: phase-A (probably plagioclase), Green: phase-B (probably Mg-Fe silicates) and yellow: phase-C (probably troilite). (c) A bird's eye view image (sample size: 56 x 60 x 59 μm).

II-1A-003-A3 (041008d): browse image, slice images, bird's eye view

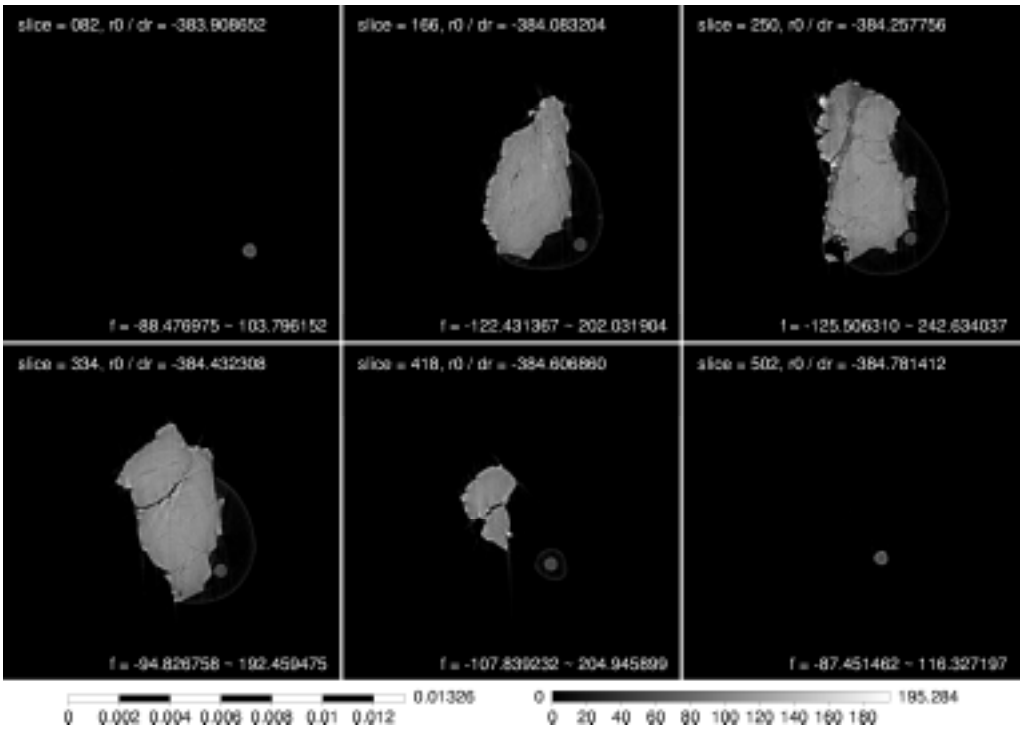

Figure 28. A browse image of CT slices of HASPET sample II-1A-003-A3 (041008d). The left and right bars are a scale bar in cm and a gray scale bar for CT values in cm^{-1}, respectively.

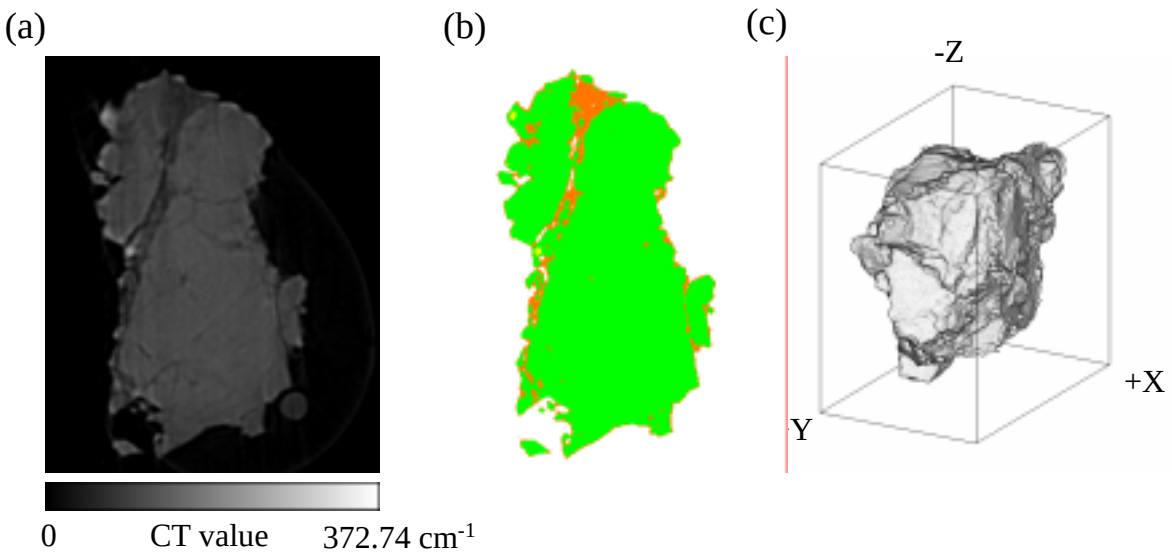

Figure 29. A typical CT slice and a bird's eye view of HASPET sample II-1A-003-A3 (041008d). (a) A CT image (372.74 cm^{-1} corresponds to PV=1380 in Figure 23. The width of the image is 62.205 μm. (b) An image showing phases. Orange: phase-A (probably plagioclase), Green: phase-B (probably Mg-Fe silicates) and yellow: phase-C (probably troilite). (c) A bird's eye view image (sample size: 52 x 76 x 76 μm).

II-1A-004-A4 (041008c): browse image, slice images, bird's eye view

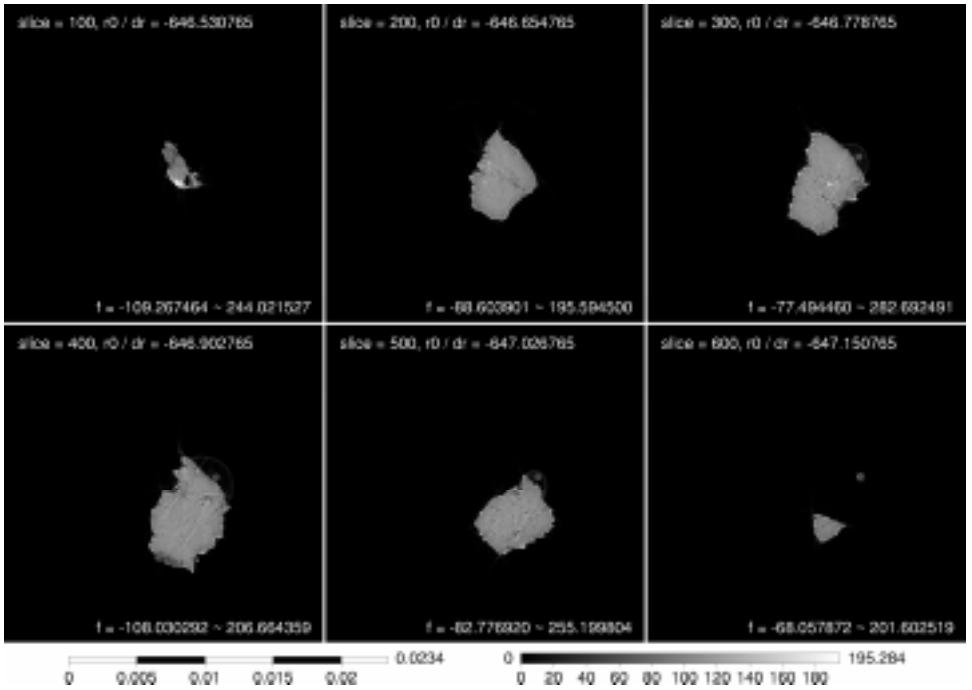

Figure 30. A browse image of CT slices of HASPET sample II-1A-004-A4 (041008c). The left and right bars are a scale bar in cm and a gray scale bar for CT values in cm^{-1}, respectively.

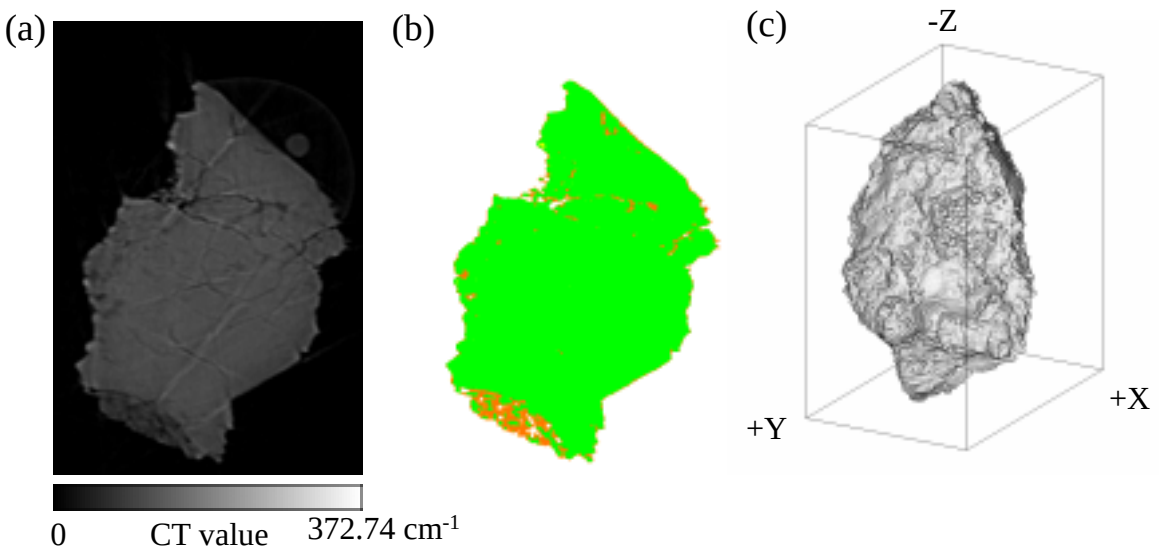

Figure 31. A typical CT slice and a bird's eye view of HASPET sample II-1A-004-A4 (041008c). (a) A CT image (372.74 cm^{-1} corresponds to PV=1380 in Figure 23. The width of the image is 69.615 μm. (b) An image showing phases. Orange: phase-A (probably plagioclase), Green: phase-B (probably Mg-Fe silicates) and yellow: phase-C (probably troilite). (c) A bird's eye view image (sample size: 69 x 101 x 117 μm).

II-1A-005-A5 (041008b): browse image, slice images, bird's eye view

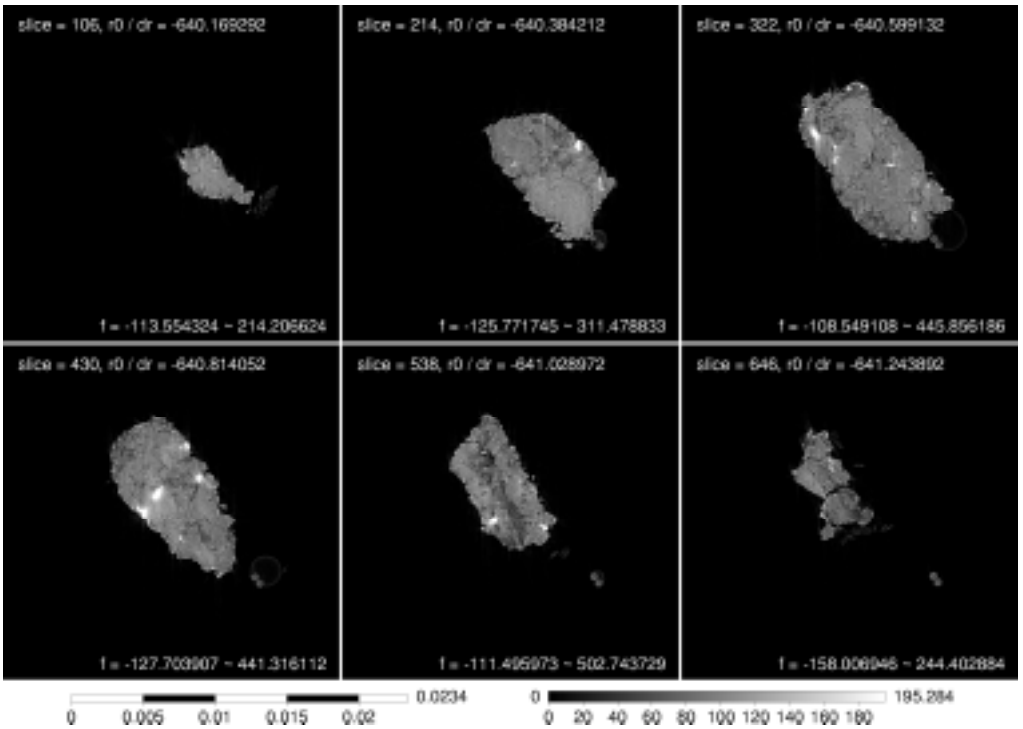

Figure 32. A browse image of CT slices of HASPET sample II-1A-005-A5 (041008b). The left and right bars are a scale bar in cm and a gray scale bar for CT values in cm^{-1}, respectively.

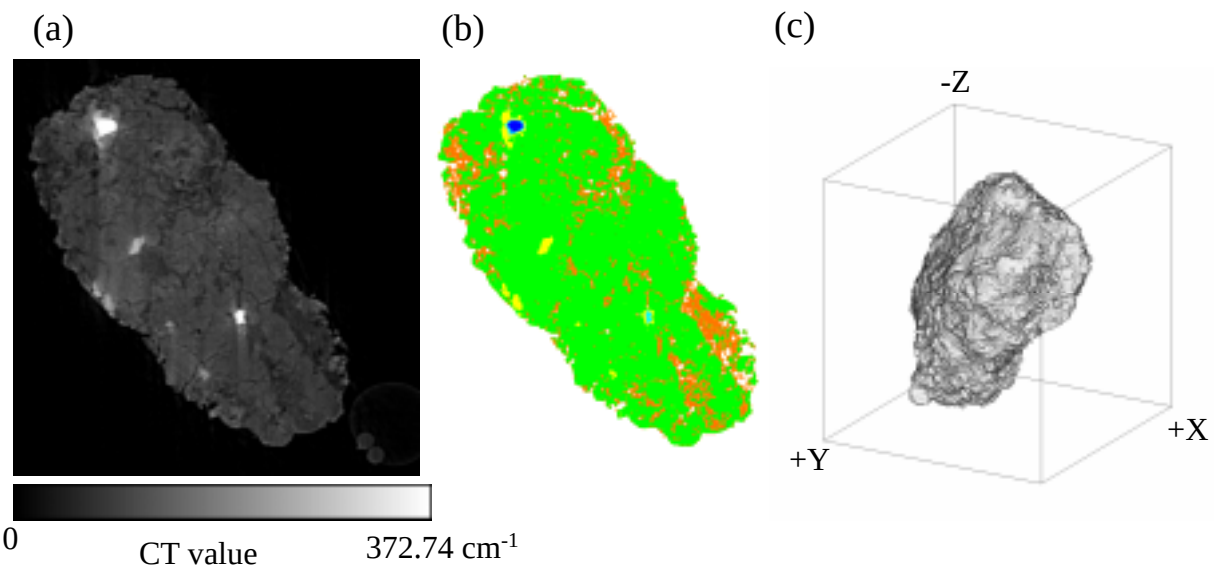

Figure 33. A typical CT slice and a bird's eye view of HASPET sample II-1A-005-A5 (041008b). (a) A CT image (372.74 cm^{-1} corresponds to PV=1380 in Figure 23. The width of the image is 122.46 μm. (b) An image showing phases. Orange: phase-A (probably plagioclase), Green: phase-B (probably Mg-Fe silicates), yellow: phase-C (probably troilite), cyan: phase-D (probably kamacite, and blue: phase-E (probably taenite). (c) A bird's eye view image (sample size: 121 x 125 x 134 μm).

II-1A-006-A6 (041008h): browse image, slice images, bird's eye view

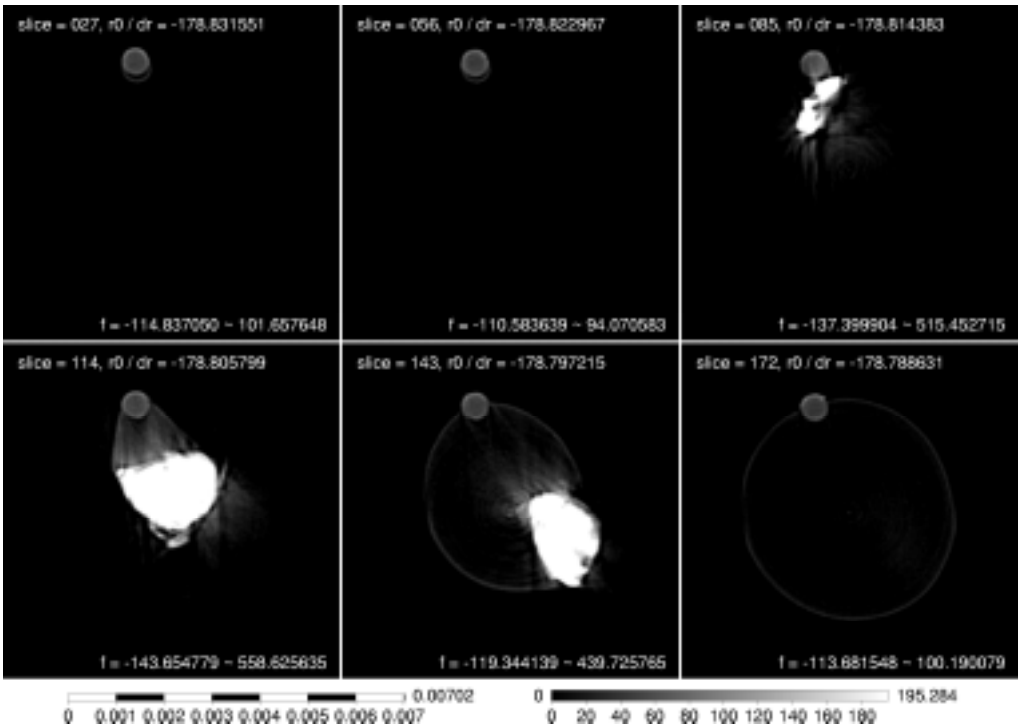

Figure 34. A browse image of CT slices of HASPET sample II-1A-006-A6 (041008h). The left and right bars are a scale bar in cm and a gray scale bar for CT values in cm^{-1}, respectively.

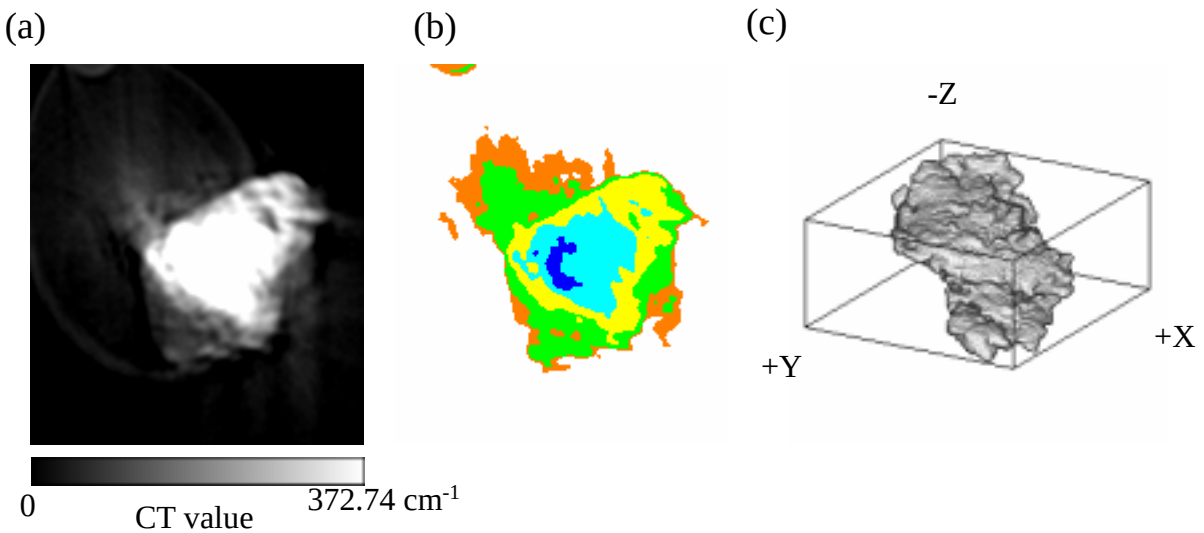

Figure 35. A typical CT slice and a bird's eye view of HASPET sample II-1A-006-A6 (041008h). (a) A CT image (372.74 cm^{-1} corresponds to PV=1380 in Figure 23. The width of the image is 32.37 μm. (b) An image showing phases. Orange: phase-A (probably plagioclase), Green: phase-B (probably Mg-Fe silicates), yellow: phase-C (probably troilite), cyan: phase-D (probably kamacite, and blue: phase-E (probably taenite). (c) A bird's eye view image (sample size: 32 x 36 x 15 μm).

II-1A-014-A14 (041008i): browse image, slice images, bird's eye view

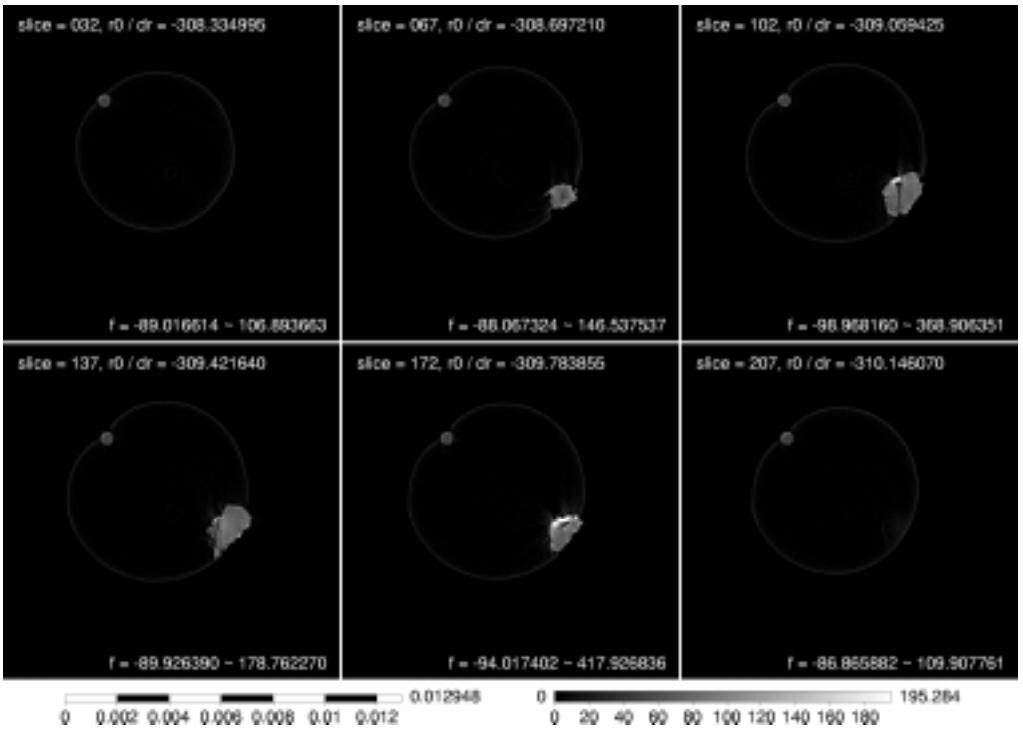

Figure 36. A browse image of CT slices of HASPET sample II-1A-0014-A14 (041008i). The left and right bars are a scale bar in cm and a gray scale bar for CT values in cm^{-1}, respectively.

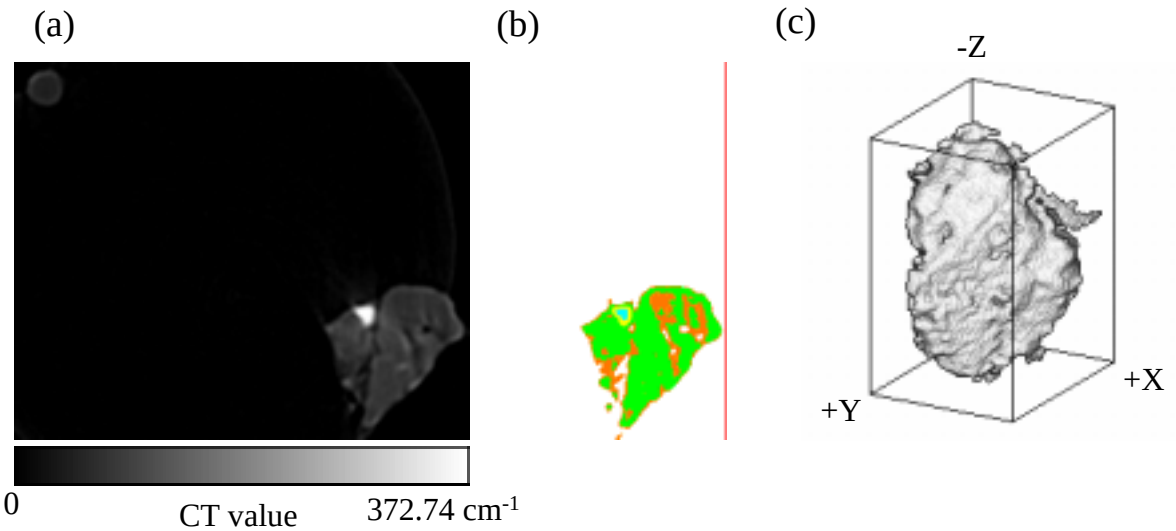

Figure 37. A typical CT slice and a bird's eye view of HASPET sample II-1A-014-A14 (041008i). (a) A CT image (372.74 cm^{-1} corresponds to PV=1380 in Figure 23. The width of the image is 60.645 μm. (b) An image showing phases. Orange: phase-A (probably plagioclase), Green: phase-B (probably Mg-Fe silicates), yellow: phase-C (probably troilite) and cyan: phase-D (probably kamacite. (c) A bird's eye view image (sample size: 19 x 24 x 33 μm).

II-1A-001 to 006, 010 (041008b, c, d, e, f, h and i): summary

Table 8. The LACs of phases-A, B, C, D and E in HASPET samples II-1A-001-A1(041008f), 002-A2 (041008e), 003-AA3 (041008d), 004-A4 (041008c), 005-A5 (041008b), 006-A6 (041008h) and 010-A14 (041008i), calculated form their CT values and estimation of their mineral candidates and compositions. LAC values of phases-C, D and E calculated form the CT values should be smaller than the real values due to their large LAC values.

	CT value (cm^{-1})	LAC (cm^{-1})	candidates		LAC (cm^{-1})		LAC (cm^{-1})		LAC (cm^{-1})
phase-A	55.4	62.6	plagioclase	An51	62.6				
phase-B (041008b)	93.5	105.6	Mg-Fe silicate	Fo87	105.8	En82	105.6		
phase-B (041008c)	100.8	113.9	Mg-Fe silicate	Fo85	113.9	En79	113.8		
phase-B (041008d)	105.1	118.7	Mg-Fe silicate	Fo84	118.7	En77	118.7		
phase-B (041008e)	93.2	105.3	Mg-Fe silicate	Fo87	105.4	En82	105.3		
phase-B (041008f)	86.4	97.7	Mg-Fe silicate	Fo89	97.7	En85	97.6		
phase-B abd C? (041008i)	74.6	84.2	silicate	An100	77.6	Fo93	84.3	En89.9	84.3
phase-B (041008bcdef)	102.9	116.3	Mg-Fe silicate	Fo84	116.3	En78	116.3		
phase-C	266.1	300.6	troilite	troilite	612.9				
phase-D	479.4	541.7	kamacite	Fe	1346.6				
phase-E	559.1	631.8	taenite	Ni	1862.2				

Table 9. The volume of HASPET samples II-1A-001-A1(041008f), 002-A2 (041008e), 003-AA3 (041008d), 004-A4 (041008c), 005-A5 (041008b), 006-A6 (041008h) and 010-A14 (041008i) and the modes of the phases.

	041008b	041008c	041008d	041008e	041008f	041008h	041008i	wt.mean	stdev	
volume (voxel)	**64796591**	**27345006**	**12766017**	**7945645**	**11071598**	**530389**	**501100**			
volume (μm^3)	**4.805E+05**	**2.028E+05**	**9.466E+04**	**5.892E+04**	**8.209E+04**	**3.933E+03**	**3.716E+03**			
mode /%										
phase-A	**16.0**	**5.0**	**5.6**	**7.8**	**15.3**	**19.5**	**28.9**	**12.0**	**5.2**	**plagioclase**
phase-B	**82.1**	**94.8**	**94.3**	**86.7**	**74.3**	**27.6**	**68.4**	**85.5**	**7.7**	**Mg-Fe silicates**
phase-C	**0.8**	**0.1**	**0.0**	**5.3**	**6.6**	**36.0**	**1.7**	**1.5**	**3.0**	**troilite**
phase-D	**0.1**	**0.0**	**0.0**	**0.0**	**3.1**	**16.3**	**0.5**	**0.4**	**1.3**	**kamacite**
phase-E	**0.0**	**0.0**	**0.0**	**0.0**	**0.0**	**0.6**	**0.0**	**0.0**	**0.0**	**taenite**
voids	**1.0**	**0.1**	**0.1**	**0.2**	**0.7**	**0.1**	**0.5**	**0.6**	**0.4**	
mass estimaged (µg)	**17.6**	**7.4**	**3.5**	**2.2**	**3.0**	**0.1**	**0.1**			

HASPET sample II-1B: OM images

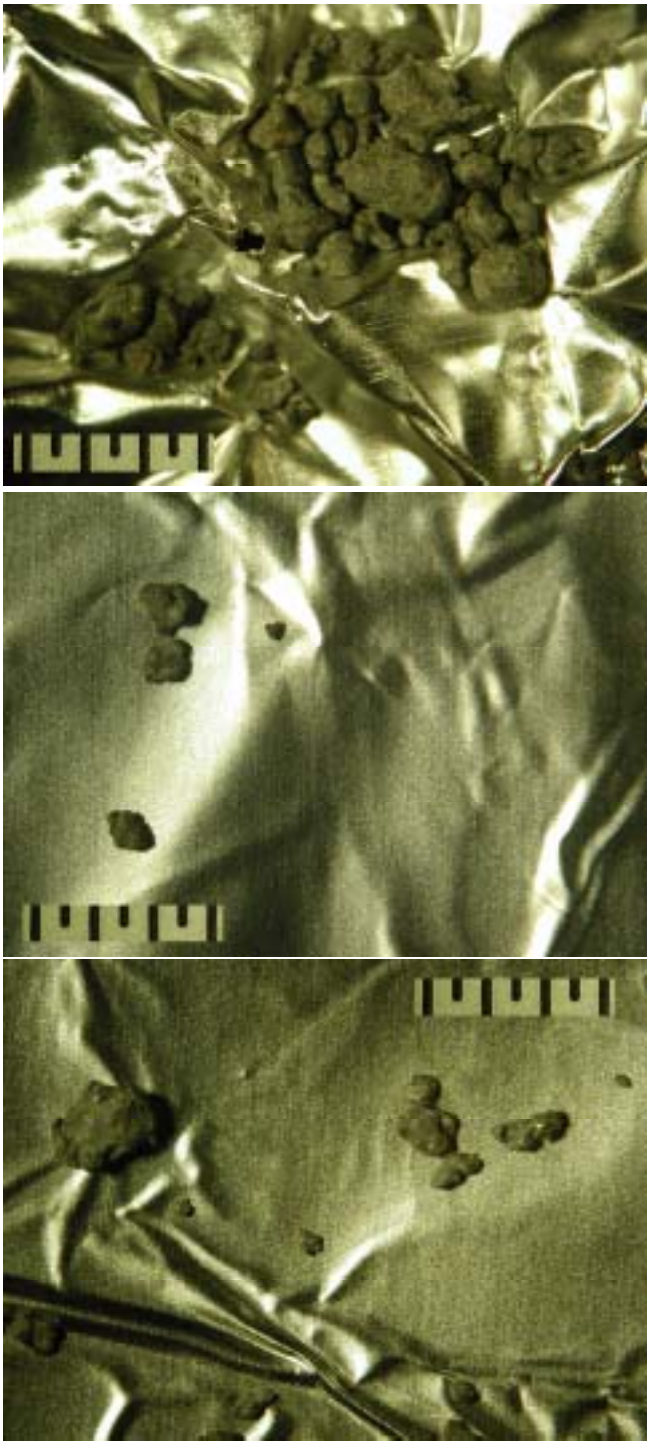

Figure 38. Photomicrographs of HASPET sample II-1B. Sample grains are on an Al foil. The separation between each scale bar is 0.5 mm.

II-1B-001, 002, 004, 008 (041007a, b, c and 041008a): OM images

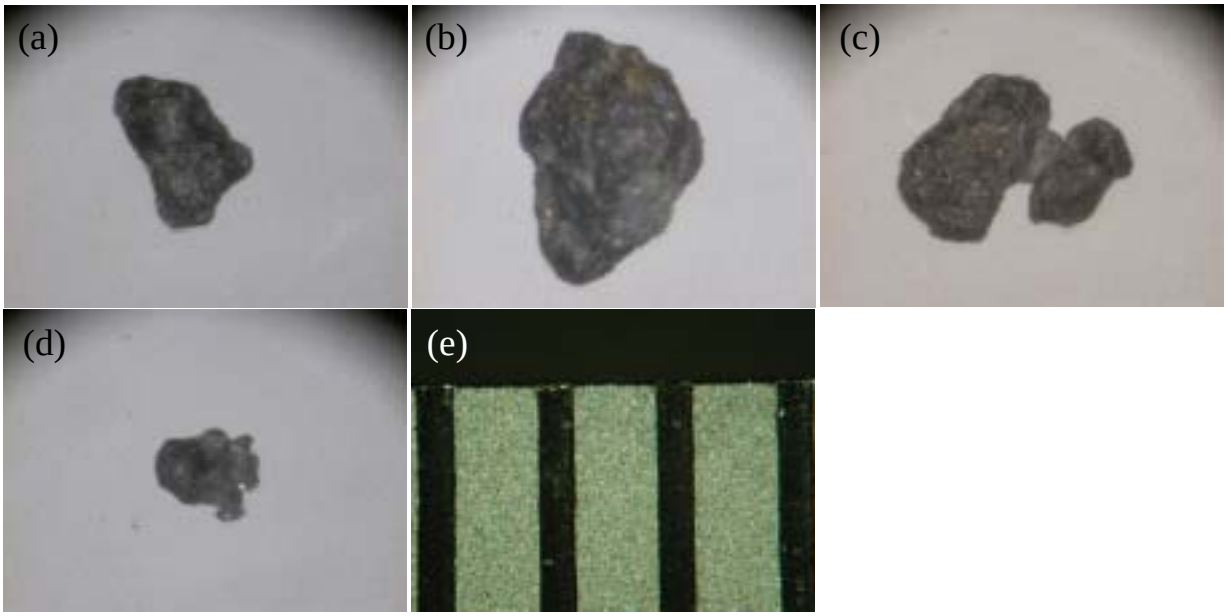

Figure 39. Photomicrograph of single grains (HASPET sample II-1B) . (a) 002-A8 (041007c). (b) 004-A10 (041007a). (c) 008-A15 (041007b). (d) 001-A7 (04108a). (e) A scale. The separation between each scale bar is 0.5 mm.

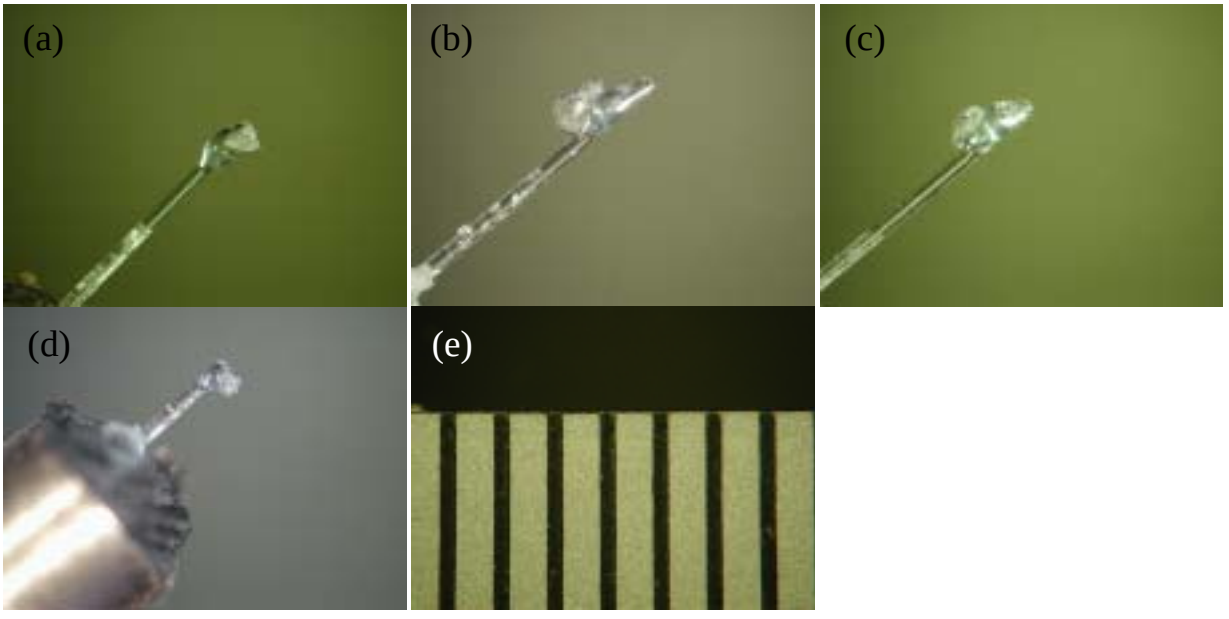

Figure 40. Photomicrograph of single grains (HASPET sample II-1B) on a glass fiber. (a) 002-A8 (041007c). (b) 004-A10 (041007a). (c) 008-A15 (041007b). (d) 001-A7 (04108a). (e) A scale. The separation between each scale bar is 0.5 mm.

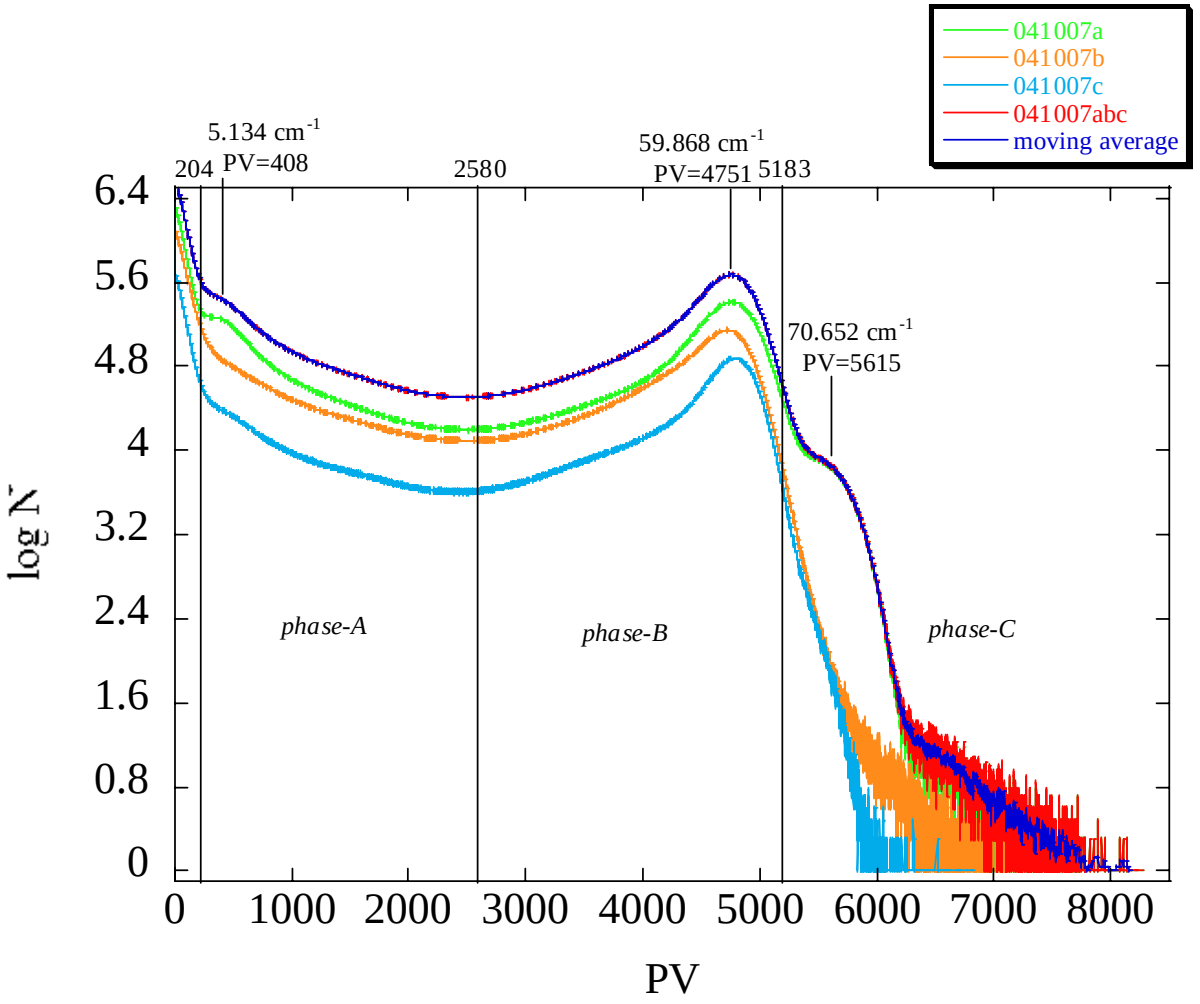

Figure 41. A CT value histogram of HASPET samples II-1B-002-A8 (041007c), 004-A10 (041007a) and 008-A15 (041007b). The CT values, *f*, are replaced by the pixel values, PV, in 16 bit images (f = 0.012583 cm^{-1} x PV). Peak PVs and CT values for phases-A, B and C, and threshold PVs between the phases are shown.

II-1B-002-A8 (041007c): browse image, slice images, bird's eye view

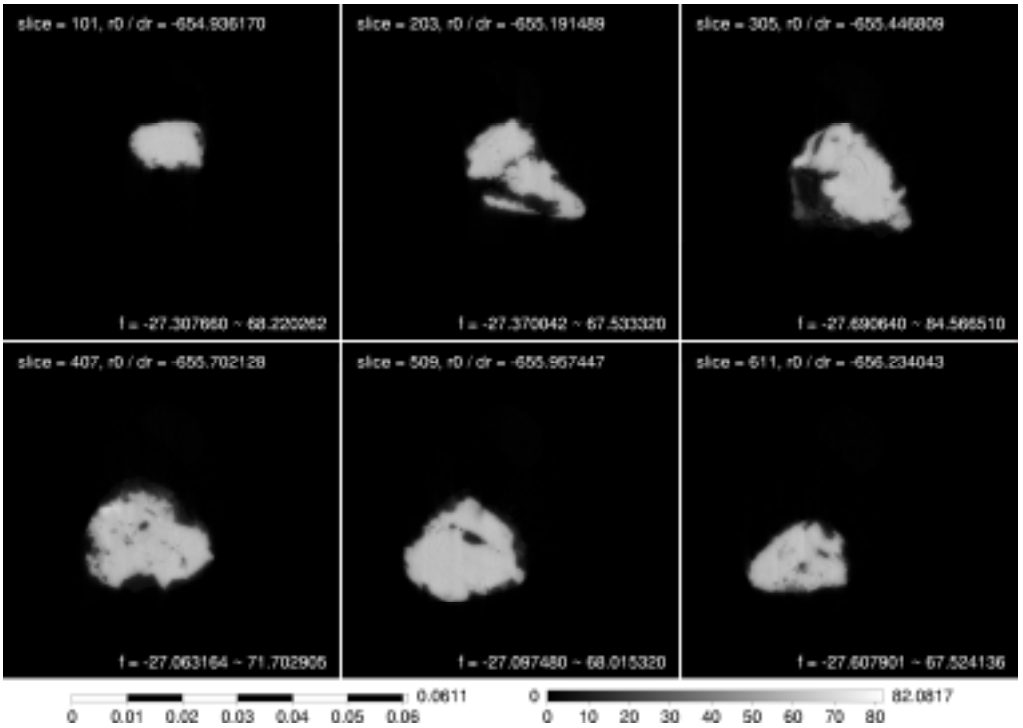

Figure 42. A browse image of CT slices of HASPET sample II-1B-002-A8 (041007c). The left and right bars are a scale bar in cm and a gray scale bar for CT values in cm^{-1}, respectively.

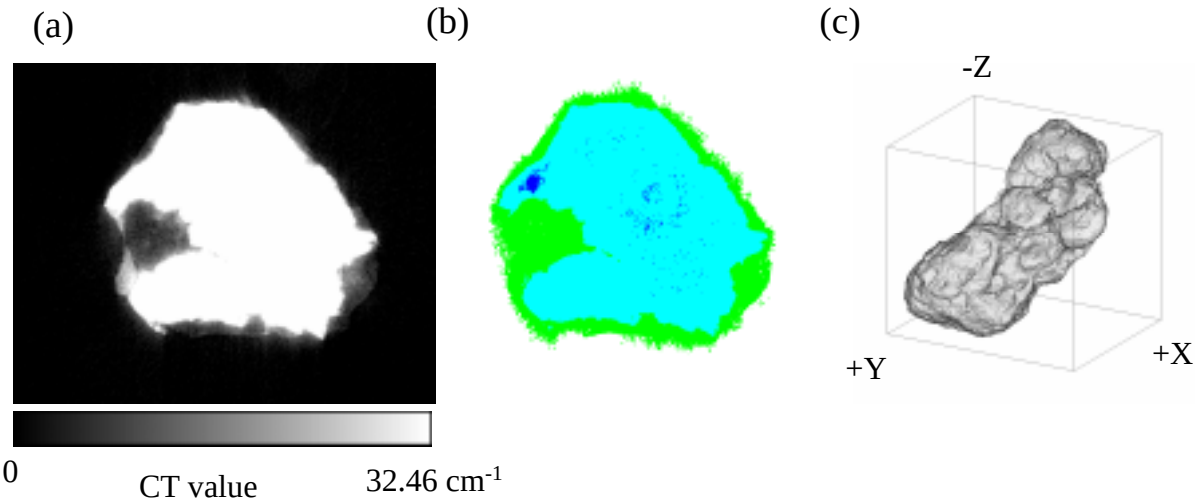

Figure 43. A typical CT slice and a bird's eye view of HASPET sample II-1B-002-A8 (041007c). (a) A CT image (32.46 cm^{-1} corresponds to PV=2580 in Figure 41). The width of the image is 344.98 μm. (b) An image showing phases. Green: phase-A (probably Mg-Fe silicates), cyan: phase-B (probably kamacite, and blue: phase-C (probably taenite). (c) A bird's eye view image (sample size: 332 x 226 x 308 μm).

II-1B-004-A10 (041007a): browse image, slice images, bird's eye view

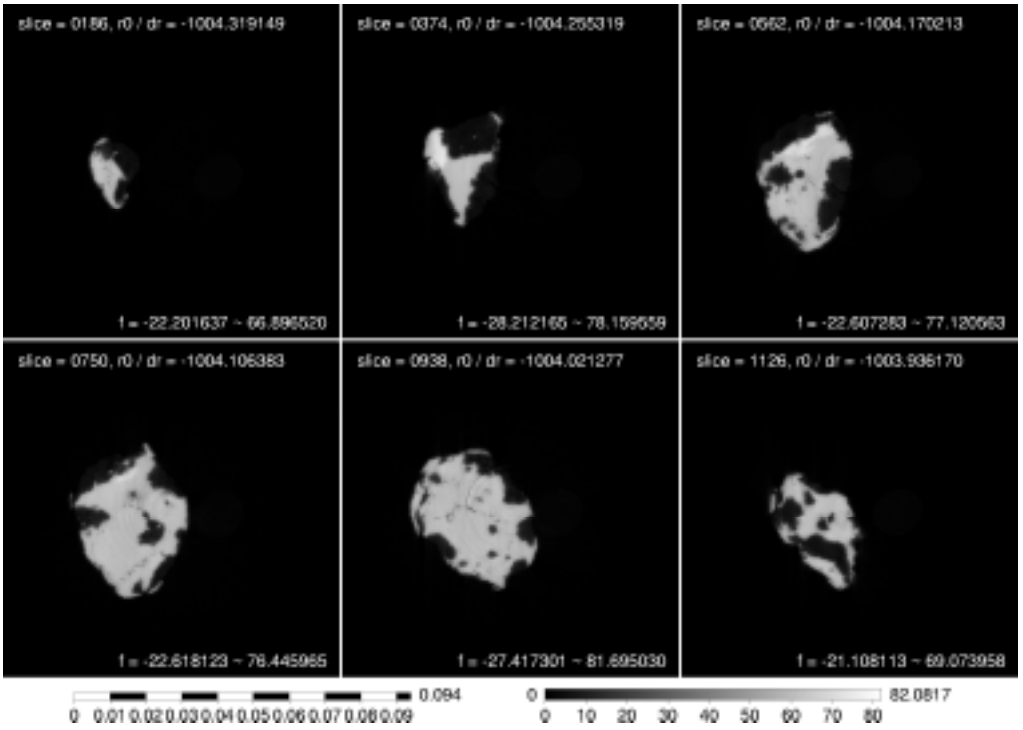

Figure 44. A browse image of CT slices of HASPET sample II-1B-004-A10 (041007a). The left and right bars are a scale bar in cm and a gray scale bar for CT values in cm^{-1}, respectively.

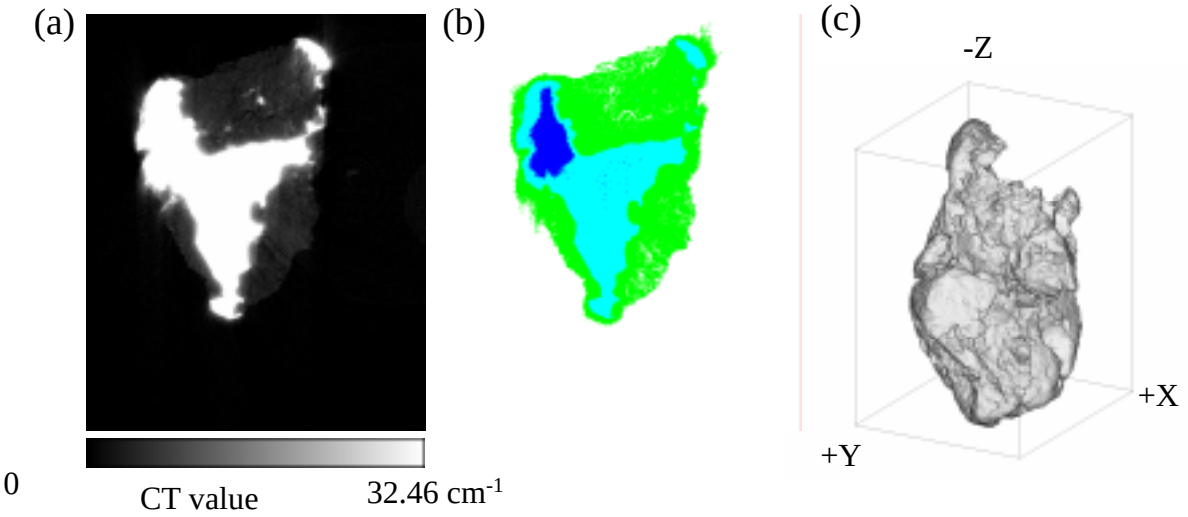

Figure 45. A typical CT slice and a bird's eye view of HASPET sample II-1B-004-A10 (041007a). (a) (32.46 cm^{-1} corresponds to PV=2580 in Figure 41). The width of the image is 383.99 μm. (b) An image showing phases. Green: phase-A (probably Mg-Fe silicates), cyan: phase-B (probably kamacite, and blue: phase-C (probably taenite). (c) A bird's eye view image (sample size: 368 x 436 x 570 μm).

II-1B-008-A15 (041007b): browse image, slice images, bird's eye view

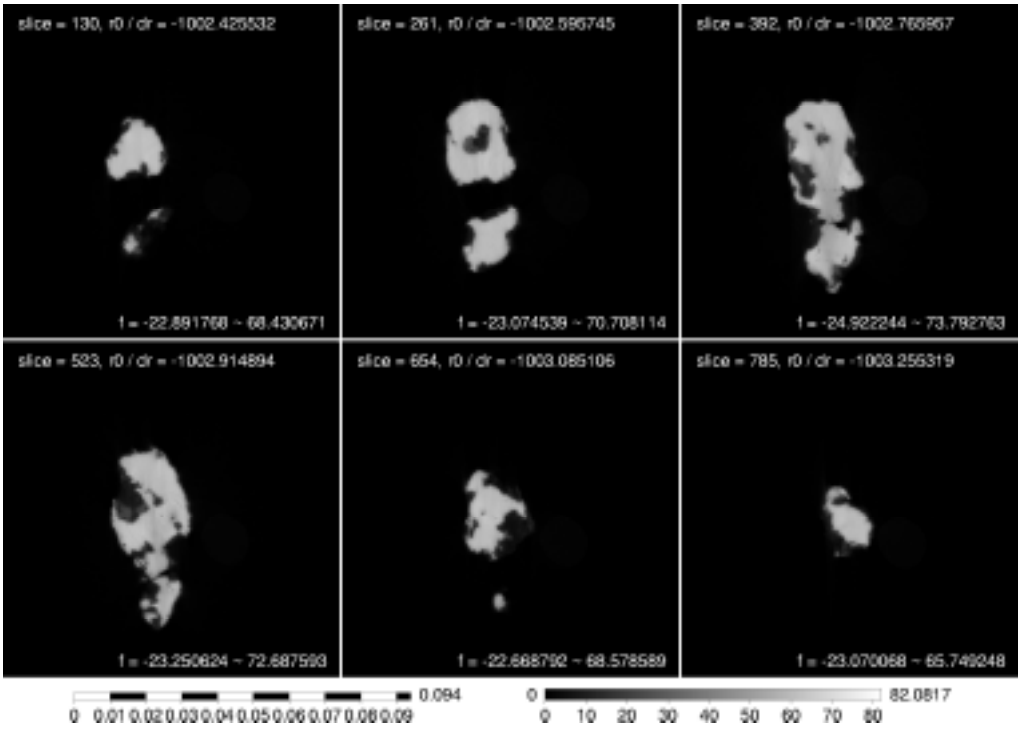

Figure 46. A browse image of CT slices of HASPET sample II-1B-008-A15 (041007b). The left and right bars are a scale bar in cm and a gray scale bar for CT values in cm^{-1}, respectively.

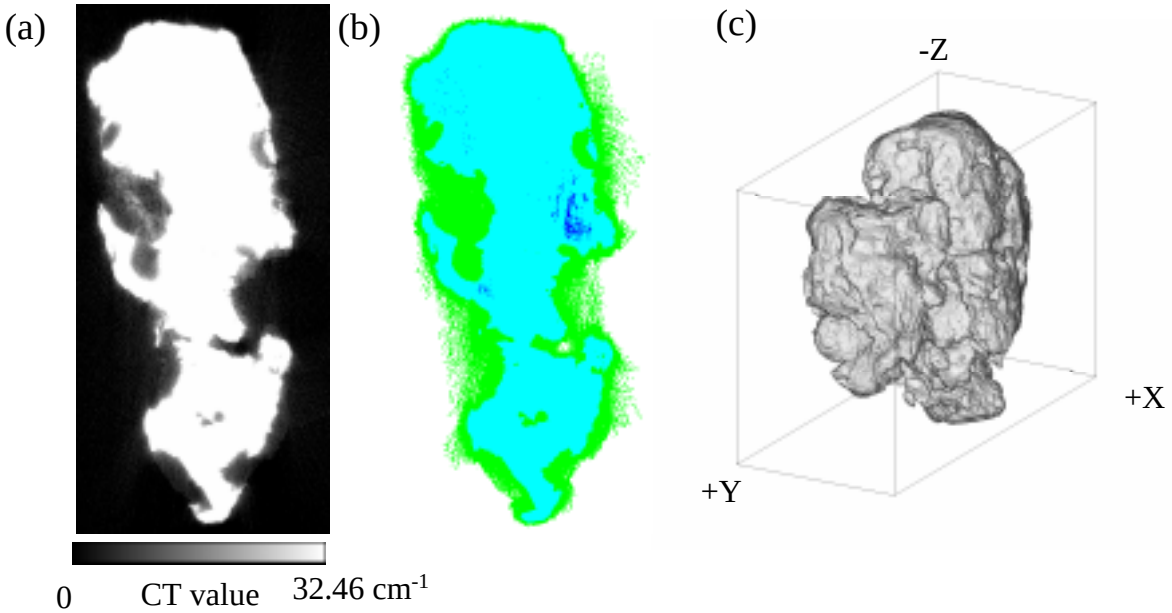

Figure 47. A typical CT slice and a bird's eye view of HASPET sample II-1B-008-A15 (041007b). (a) A CT image (32.46 cm^{-1} corresponds to PV=2580 in Figure 41). The width of the image is 272.6 μm. (b) An image showing phases. Green: phase-A (probably Mg-Fe silicates), cyan: phase-B (probably kamacite, and blue: phase-C (probably taenite). (c) A bird's eye view image (sample size: 252 x 599 x 405 μm).

II-1B-002, 004, 008 (041007a, b and c): summary

Table 10. The LACs of phases-A, B and C in HASPET samples II-1B-002-A8 (041007c), 004-A10 (041007a) and 008-A15 (041007b)., calculated form their CT values and estimation of their mineral candidates and compositions.

	CT value (cm^{-1})	LAC (cm^{-1})	candidate		LAC (cm^{-1})		LAC (cm^{-1})
phase-A	5.13	5.80	silicate	Fo83	5.80	En76.1	5.81
phase-B	59.87	67.65	kamacite	Fe88	67.64		
phase-C	70.65	79.83	taenite	Fe43	79.83		

Table 11. The volume of HASPET samples II-1B-002-A8 (041007c), 004-A10 (041007a) and 008-A15 (041007b) and the modes of the phases.

	041007a	041007b	041007c	wt.mean		
sample(mg)	0.2400	0.1344	0.0576			
stdev	0.0004	0.0007	0.0011			
volume (voxel)	336716996	195684963	77218257			
volume (cm3)	3.496E-05	2.032E-05	8.017E-06			
density (g/cm3)	6.87	6.62	7.18	6.89		
stdev	0.01	0.03	0.14	0.29		
mode (%)						candidates
phase-A	38.9	38.3	30.6	37.7	2.7	silicates
phase-B	61.1	61.7	69.4	62.3	2.7	metal
phase-C	59.6	61.6	69.1	61.4	3.1	kamacite
phase-D	1.5	0.2	0.2	0.9	0.7	taenite

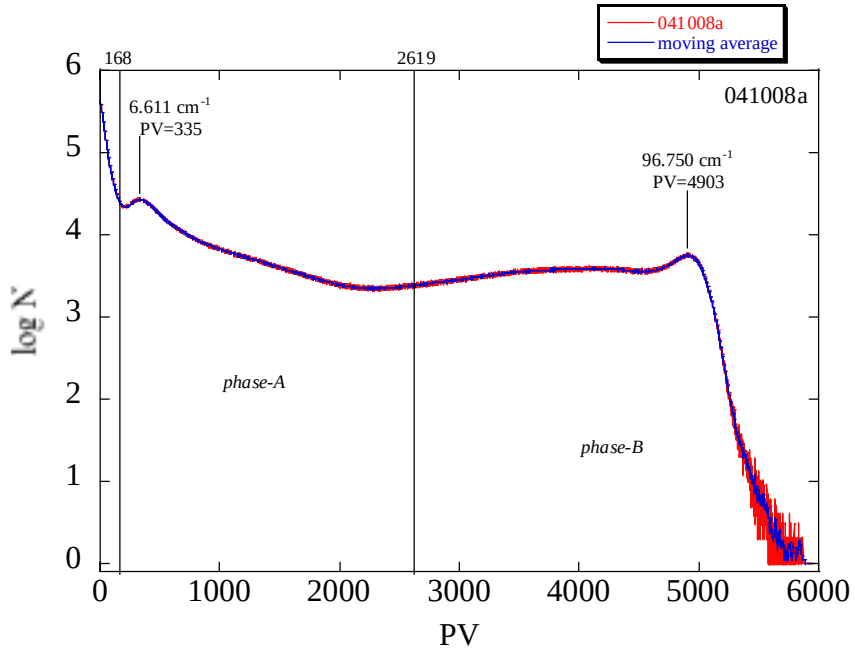

Figure 48. A CT value histogram of HASPET sample II-1B-001-A7 (041008a). The CT values, *f*, are replaced by the pixel values, PV, in 16 bit images (f = 0.019733 cm^{-1} x PV). Peak PVs and CT values for phases-A, B and C, and threshold PVs between the phases are shown.

Table 12. The LACs of phases-A and B in HASPET sample II-1B-001-A7 (041008a) calculated form their CT values and estimation of their mineral candidates and compositions.

	CT value (cm^{-1})	LAC (cm^{-1})	candidate			LAC (cm^{-1})		LAC (cm^{-1})
phase-A	6.61	7.47	Mg-Fe silicates	Fo89	7.47	En85	7.47	
phase-B	96.75	109.32	kamacite	Fe97	109.34			

Table 13. The volume of HASPET sample II-1B-001-A7 (041008a) and the modes of the phases.

	041009def	
sample(mg)	0.0144	
stdev	0.0009	
volume (cm^3)	2.847E-06	
density (g/cm^3)	5.05	
stdev	0.32	
mode (%)		candidate
phase-A	67.3	Mg-Fesilicates
phase-B	32.7	metal

II-1B-001-A7 (041008a): browse image, slice images, bird's eye view

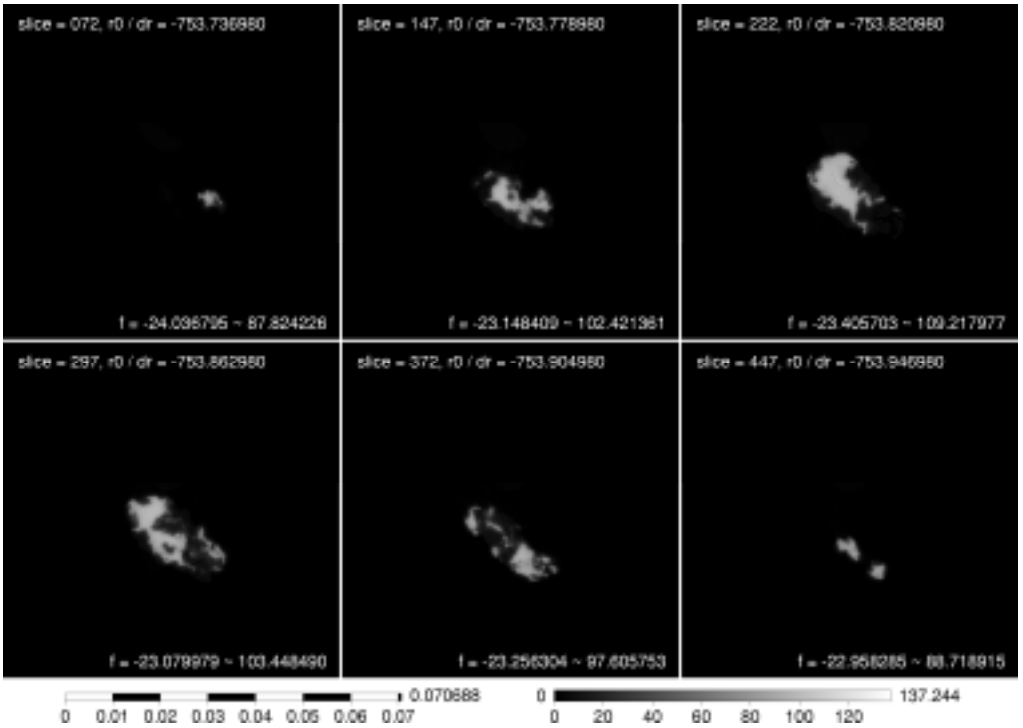

Figure 48. A browse image of CT slices of HASPET sample II-1B-001-A7 (041008a). The left and right bars are a scale bar in cm and a gray scale bar for CT values in cm^{-1}, respectively.

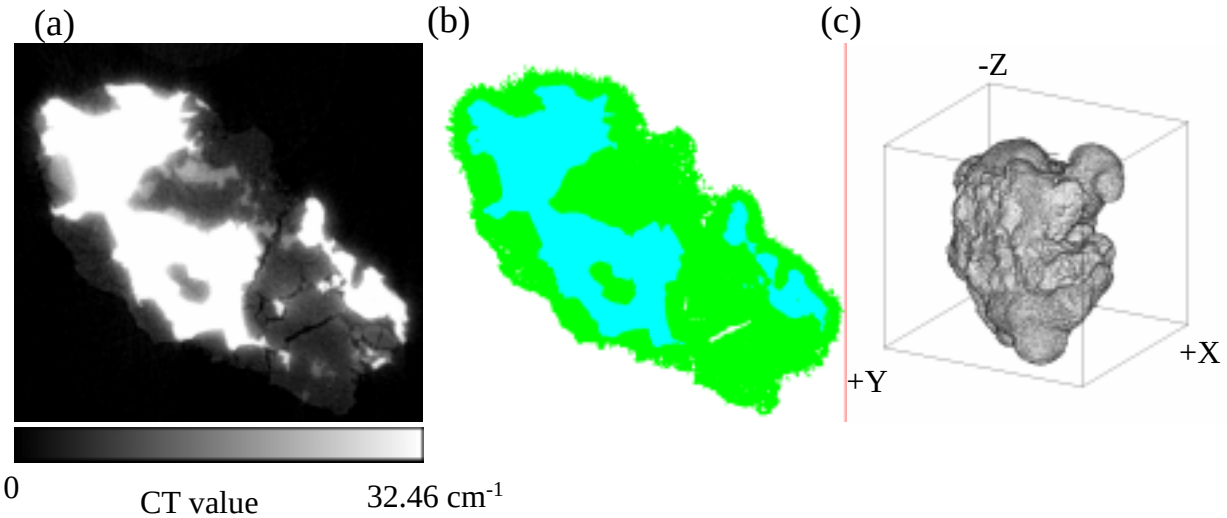

Figure 49. A typical CT slice and a bird's eye view of HASPET sample II-1B-001-A7 (041008a). (a) A CT image (32.46 cm^{-1} corresponds to PV=2580 in Figure 41). The width of the image is 227.95 μm. (b) An image showing phases. Green: phase-A (probably Mg-Fe silicates), cyan: phase-B (probably kamacite, and blue: phase-C (probably taenite). (c) A bird's eye view image (sample size: 227 x 210 x 215 μm).

HASPET sample II-1A-P3 and P4z (041010a): OM images

(a)

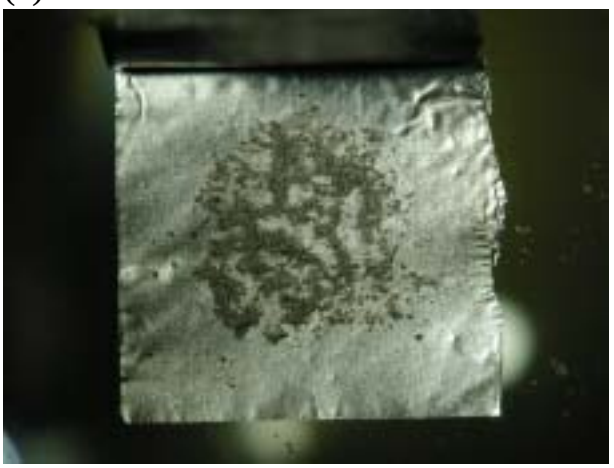

II-1A-P3_x10.JPG

(b)

II-1A-P4z_zr_x10.JPG

(c)

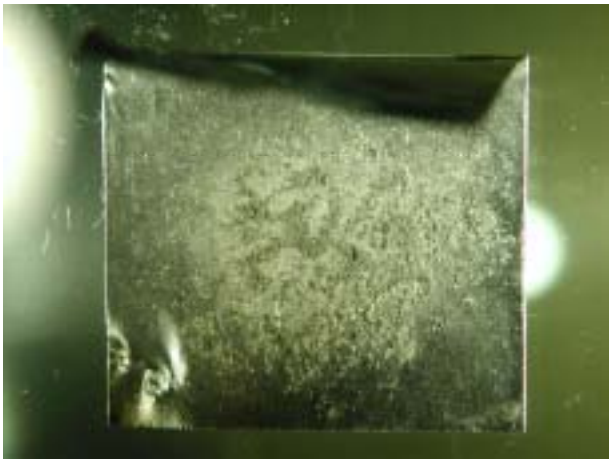

II-1A-P4z_x10.JPG

(d)

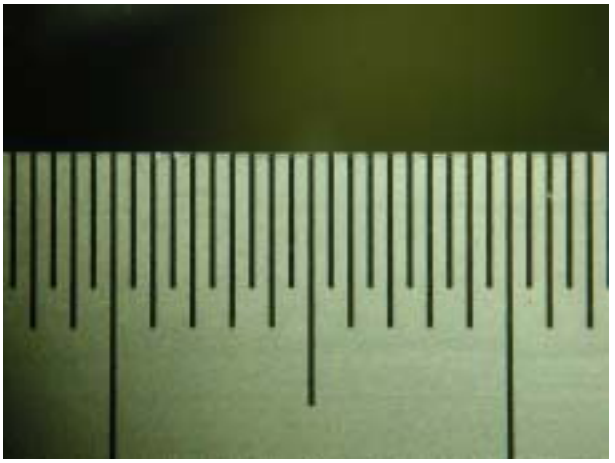

scale_x10-2.JPG (0.5 mm)

Figure 50. Photomicrographs of HASPET sample II-1A-P3 and P4z (041010a) for zircon serach. (a) A powder sample of II-1A-P3, where zircon crystals are not added, on an Al foil. (b) A powder sample of II-1A-P4z, where zircon crystals are added, on an Al foil. (c) II-1A-P4z sandwiched between Al foils. (d) A scale for (a), (b) and (c). The separation between each scale bar is 0.5 mm.

HASPET sample II-1A-P3 and P4z (041010a): mosaic projection images

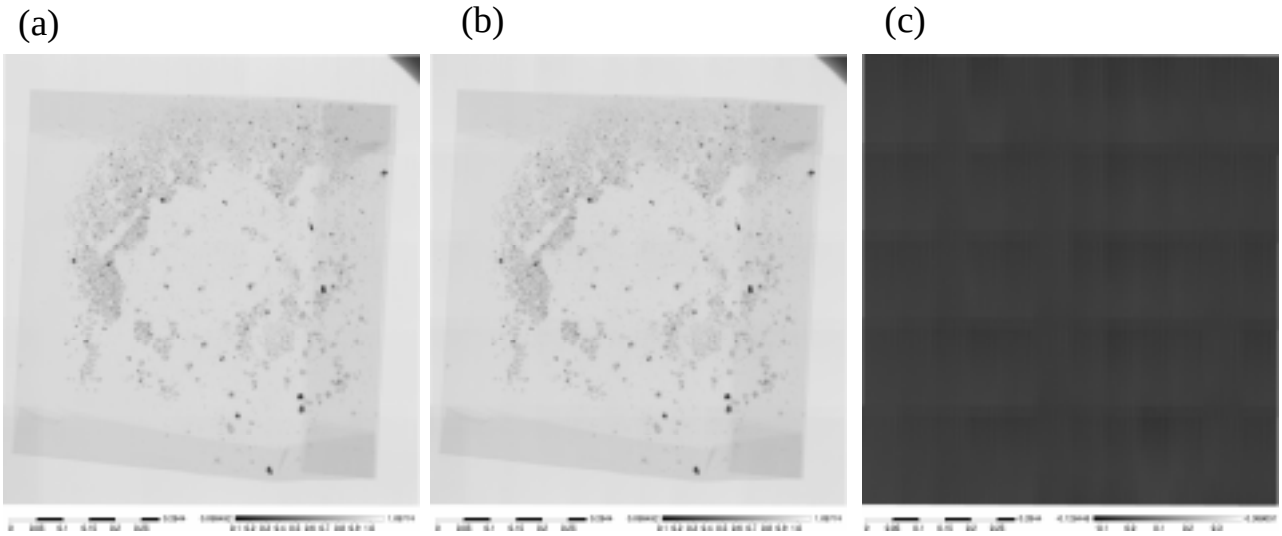

Figure 51. Mosaic projection images of HASPET sample II-1A-P3 (without zircon). The left and right bars are a scale bar in cm and a gray scale bar for transmittance, respectively. (a) Above the Zr K-edge energy. (b) Below the Zr K-edge energy. © Subtraction image. Zr-bearing minerals are not seen in this sample.

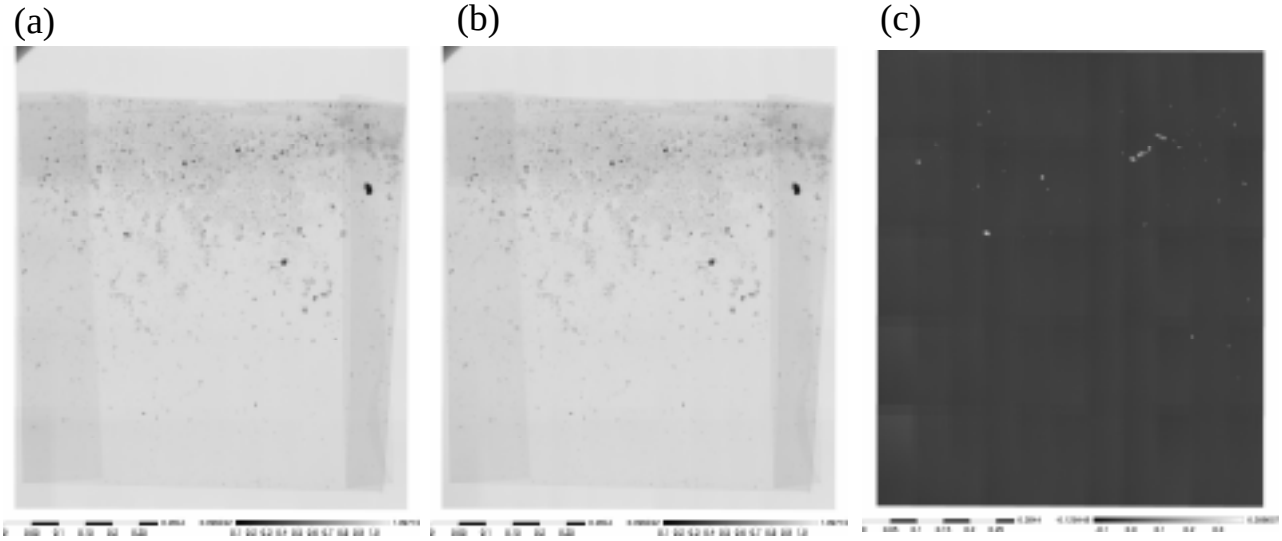

Figure 5. Mosaic projection images of HASPET sample II-1A-P4z (with zircon). The left and right bars are a scale bar in cm and a gray scale bar for transmittance, respectively. (a) Above the Zr K-edge energy. (b) Below the Zr K-edge energy. (c) Subtraction image. Zircon grains are recognized as bright spots.

HASPET sample II-1A-P4z (041010a): stereograph

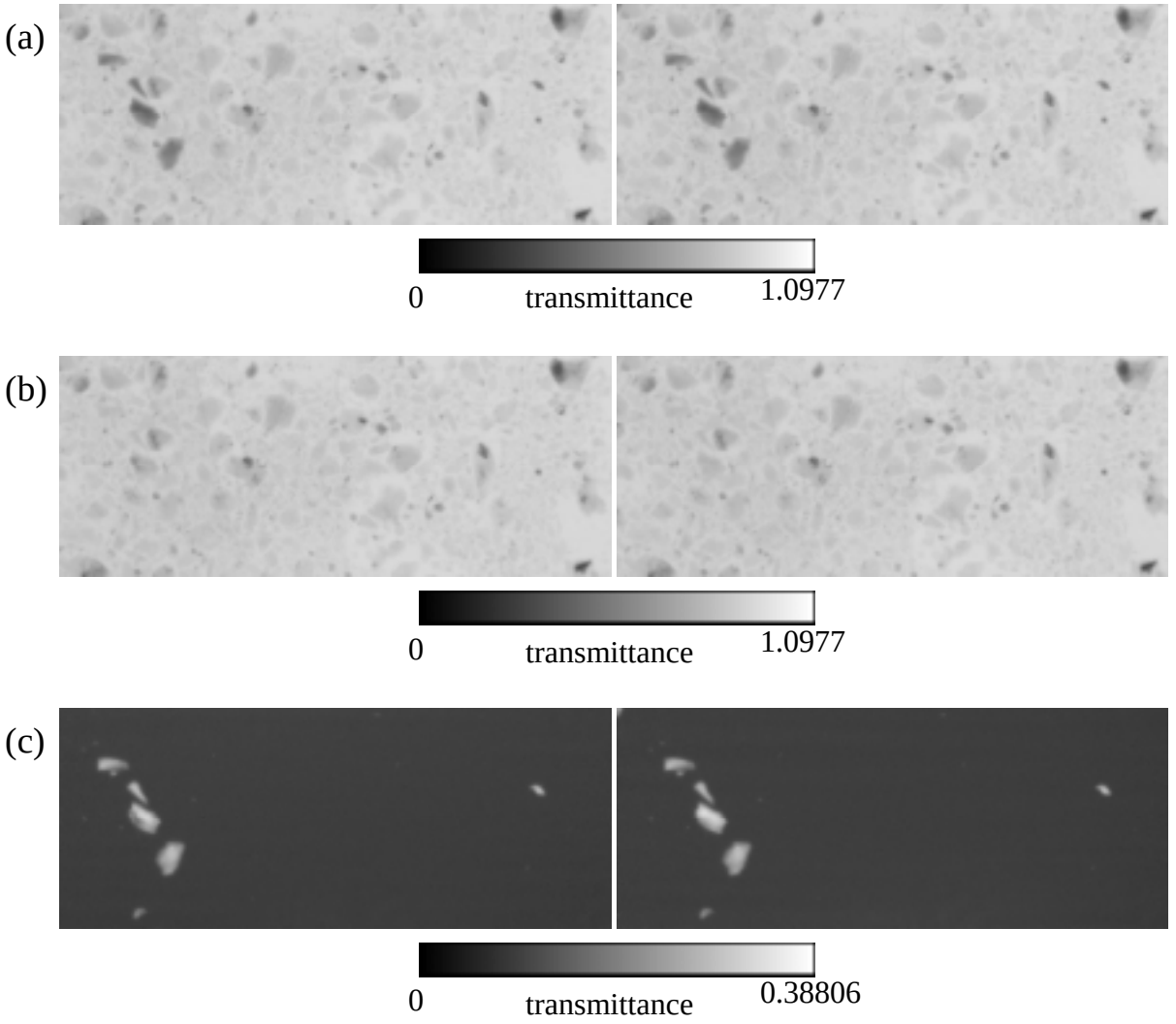

Figure 53. Stereographs for a projection images of HASPET sample II-1A-P4z (with zircon) imaged above the Zr K-edge energy. (a) Above the Zr K-edge energy. (b) Below the Zr K-edge energy. (c) Subtraction image. Gray scales are for transmission rates. The width of each projection image is 1.896 μm.

Appendix: CT value –LAC realtion

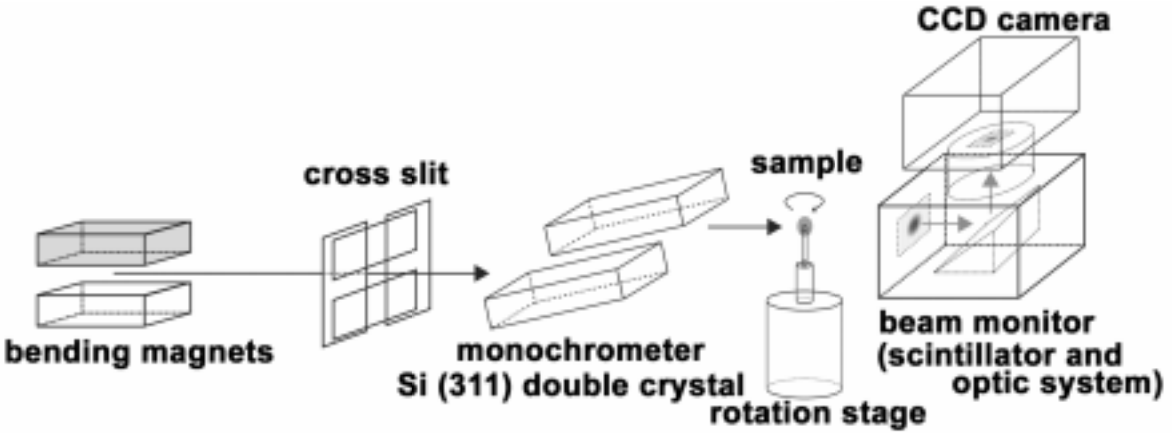

Figure A1. The schematic illustration of a projection microtomographic system at SPring-8 (Tsuchiyama et al., 2005).

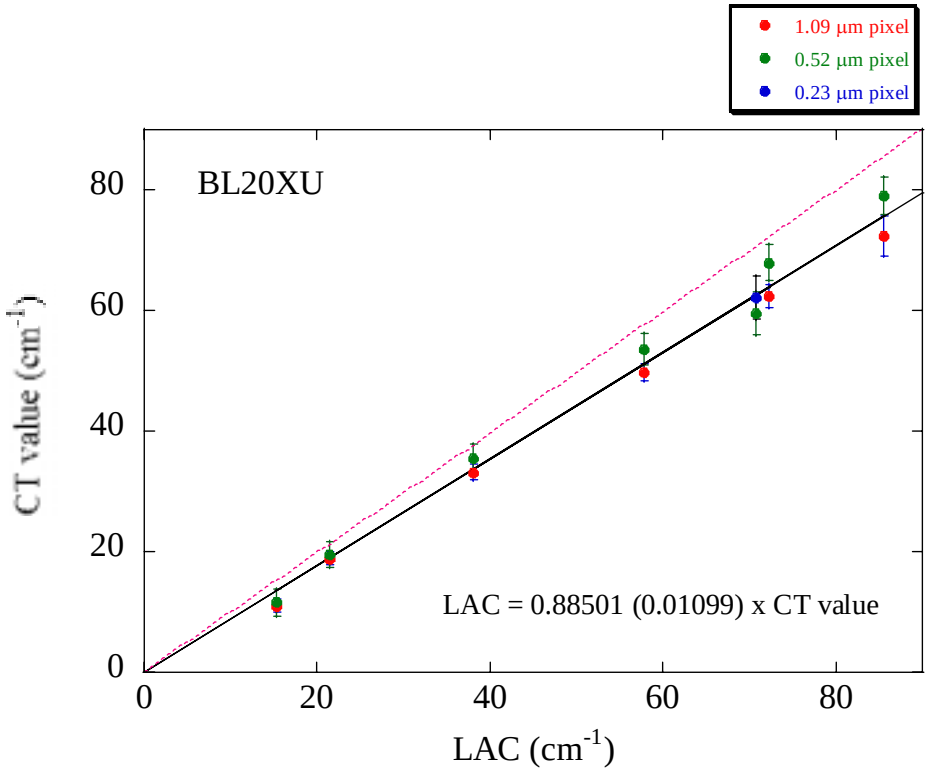

Figure A2. The relation between CT values and LAC determined by imaging standard materials at BL20XU (Nakamura et al., 2005)